

Diffusive dynamics of a model protein chain in solution

Margarita Colberg^{a)} and Jeremy Schofield^{b)}

Chemical Physics Theory Group, Department of Chemistry, University of Toronto, Toronto, Ontario M5S 3H6, Canada

(Dated: 6 February 2024)

A Markov state model is a powerful tool that can be used to track the evolution of populations of configurations in an atomistic representation of a protein. For a coarse-grained linear chain model with discontinuous interactions, the transition rates among states that appear in the Markov model when the monomer dynamics is diffusive can be determined by computing the relative entropy of states and their mean first passage times, quantities that are unchanged by the specification of the energies of the relevant states. In this paper, we verify the folding dynamics described by a diffusive linear chain model of the crambin protein in three distinct solvent systems, each differing in complexity: a hard-sphere solvent, a solvent undergoing multi-particle collision dynamics, and an implicit solvent model. The predicted transition rates among configurations agree quantitatively with those observed in explicit molecular dynamics simulations for all three solvent models. These results suggest that the local monomer-monomer interactions provide sufficient friction for the monomer dynamics to be diffusive on timescales relevant to changes in conformation. Factors such as structural ordering and dynamic hydrodynamic effects appear to have minimal influence on transition rates within the studied solvent densities.

I. INTRODUCTION

The study of the dynamics of protein folding *in silico* is challenging not only due to the complexity and size of biomolecular systems but also because of the separation of timescales between the dynamics of molecular motion and the timescales of the significant conformational motions that are important to their function. For atomistic models in which the constituents interact via molecular mechanical force fields, the potential energy landscape is typically rugged, characterized by many local minima corresponding to multiple metastable molecular configurations in which the system remains for extended periods. In brute force molecular dynamics (MD) simulations, the equations of motion must be numerically integrated with a small time step to resolve motion on the femtosecond timescale and conserve energy, while the conformational changes in a protein folding process occur on the order of nanoseconds or longer^{1,2}. Therefore, millions to billions of time steps are required for an MD simulation to witness even a single major structural change^{1,3}. Such timescales are inaccessible even with supercomputers such as Anton^{3,4}.

Markov state models (MSMs) have emerged as a popular approach to bridge this timescale gap by predicting long timescale dynamics based on numerous short MD trajectories⁵⁻⁹. In an MSM, the conformational space is partitioned into metastable states, such that intrastate transitions are fast but interstate changes are slow. The dynamics of populations in the targeted states over long times are predicted by a Markovian master equation governed by a matrix of transition rates among them. The discovery of the appropriate number and specification of

the metastable states, a critical component of the construction of an MSM, has attracted much attention, and recent advances in machine learning methods have been used to facilitate these tasks^{9,10}. After identifying the states, the transition rate matrix must be estimated using MD trajectories among any dynamically connected states^{5,11-13}. Once this transition matrix is available, the MSM can be analyzed to predict several interesting properties. For example, the probability of particular mechanistic paths starting from an initial distribution of states to the folded state can be studied to find dominant folding pathways and potential bottlenecks in the non-equilibrium folding process^{14,15}. However, because the computed rate matrix is based on explicit simulations of the system, it only applies to the conditions under which the trajectories were performed, such as the temperature and the specific force field. As such, the study of how temperature or mutations in sequence might change the folding dynamics and its pathways requires reidentification of the target states and reconstruction of the transition rate matrix.

Markov state models of simple coarse-grained protein systems can bypass these restrictions to address how interaction energies should be chosen to optimize specific dynamical properties and to elucidate how folding pathways for a given model change with temperature¹⁶. Additionally, detailed questions concerning the nature of the free energy landscape can be analyzed^{17,18}. If the bonds in the secondary or tertiary structure of the protein are modeled using attractive step potentials while all other interactions are taken to be hard-core repulsions, the point at which bond formation or breaking occurs is defined geometrically. The configurational space can be partitioned into non-overlapping regions, each corresponding to a particular configuration or bonding pattern in the protein. A dimensionless entropy can be determined for each configuration, dependent only on the distances between the protein's monomers and independent

^{a)} Electronic mail: margarita.gladkikh@mail.utoronto.ca

^{b)} Electronic mail: jeremy.schofield@utoronto.ca

of its energy. Using this entropy, the canonical probability of a configuration can be easily determined for any temperature and bonding energy. Consequently, the impact of the choice of temperature and bonding energies in the model on measures of the roughness of the free energy landscape can be examined¹⁷.

Previously¹⁶, the dynamics of a protein-like chain were modeled using an MSM in which the elements of the transition rate matrix were predicted from a kinetic model that assumes diffusive monomer dynamics. In the simple model, the rates of transitions between states, defined in terms of the distances of a set of nonlocal contacts, can be computed primarily from geometrical information, namely, the configurational entropy and the mean squared diffusion distance between states, which are readily obtained from importance sampling calculations that do not require simulating the real dynamics. In Ref. (16), importance sampling was performed using hybrid Monte Carlo¹⁹ based on artificial event-driven dynamical trajectories. When bonding interactions are in the form of step potentials, the diffusion coefficient along a bonding reaction coordinate, needed to scale the mean squared diffusion distance to compute mean first passage times, can also be computed from the sampling trajectories. Since the kinetic model provides analytical expressions for the transition rate matrix in terms of these quantities and the choice of state energies relative to the temperature, dynamical characteristics of the protein-like chain, such as the mean transition time between extended and native-like configurations, can be predicted and optimized with respect to the choice of state energies.

The kinetic model, which underlies predictions, is based on a number of assumptions that can be tested by comparing the predicted dynamics to those observed in explicit simulations. This comparison can be accomplished by estimating the transition rate matrix using any of the methods applied to extract rates from MD trajectories of systems interacting with continuous force fields^{5,12,13}. In this work, the predicted dynamics of a diffusive MSM of a linear chain model of the crambin protein suspended in a solvent bath are compared to those observed in molecular dynamics simulations. The solvents considered here interact with the monomers of the chain via either hard or effective interactions that do not alter the configurational entropy or the probability of configurations. Since the simulation of the dynamics in the presence of many solvent particles is computationally expensive, the dynamics of selected transitions in the crambin model are analyzed. The transition rate matrix elements for the selected states are determined for three solvent models of differing complexity: one implicit and two explicit. In the implicit solvent model, called the penetrating solvent, the presence of the solvent is mimicked by a periodically applied stochastic random force to the monomers. This solvent is the least computationally expensive, and the method is essentially equivalent to Brownian dynamics simulations for event-driven dy-

namics. The penetrating solvent provides a stochastic environment for the chain to allow thermal equilibration but does not include hydrodynamic flow. The two explicit solvents are modeled using multi-particle collision dynamics (MPCD) with hard interactions and a hard-sphere fluid. Both solvent models allow for hydrodynamic flow, and the latter takes into consideration the structure of the solvent around the chain.

We find that the dynamics predicted by the diffusive MSM are in good agreement with the dynamics observed in all three solvent models, even at low densities with relatively large monomer self-diffusion coefficients. These results suggest that the internal friction arising from the elastic collisions of monomers due to excluded volume and local geometric constraints that maintain the linear chain provides sufficient dissipation, when combined with weak solvent collisions, to establish a separation of timescale between the timescale of bond forming and breaking events and the decorrelation time of bead velocities. Furthermore, for the solvent densities studied here, hydrodynamic flow and solvent structure are not significant in determining the transition rates.

The outline of this paper is as follows: In Sec. II, we introduce the coarse-grained model, followed by a description of the specific interactions chosen to represent crambin in Sec. II A. The configurational entropy and the canonical probability of macrostates are briefly discussed in Sec. II B, after which the transition rate matrix elements of the diffusive MSM and the mean first passage times are presented in Sec. II C. In Sec. II D, the layer method is briefly reviewed, which is an approach developed previously¹⁶ to compute the rate of transitions between intermediate states in a massively parallel way. Sec. II E concludes this section by discussing the diffusion coefficient needed to evaluate the mean first passage times. The three solvent bath models are introduced in Sec. III, followed by a discussion of the simulation parameters and their values in Sec. IV. In Sec. V, ten representative transitions between crambin's intermediate states are selected, and the method by which the diffusion coefficient for each transition was extracted from the simulations is outlined in Sec V A. The equilibrium probability and decay rate for crambin suspended in each of the three solvent baths were obtained and compared to the canonical probability and transition rate predicted by the diffusive MSM. Finally, results and concluding remarks are provided in Secs. VI and VII, respectively. Additional background on the derivation of the diffusive Markov state model is presented in the Appendix.

II. THE COARSE-GRAINED MODEL OF PROTEINS

The system of interest comprises a coarse-grained protein-like chain immersed in a fluid in thermal equilibrium at temperature T . Each bead in the linear chain in the model represents each amino acid in the primary structure, and connective bonds between the beads are

maintained using a square-well potential,

$$U_{ij}(r) = \begin{cases} 0 & \text{if } \sigma_1 < r < \sigma_2, \\ \infty & \text{otherwise,} \end{cases} \quad (1)$$

where r is the distance between the nearest or next-nearest neighboring beads, and σ_1 and σ_2 define the minimum and maximum bonding distances. For the nearest neighbors in the chain, $\sigma_1 = 1$, which is defined to be the unit of length ℓ in the model, and $\sigma_2 = 1.17$, whereas for the next-nearest neighbors, $\sigma_1 = 1.4$ and $\sigma_2 = 1.67$ to confine the bond angles to the range 75° – 112° . Nonlocal bonding interactions, which can occur between monomers separated by more than two beads, are modeled using a square-well potential,

$$U_{ij}(r) = \begin{cases} \infty & \text{if } r < r_h \\ \epsilon_{ij} & \text{if } r_h \leq r \leq r_c \\ 0 & \text{if } r > r_c. \end{cases} \quad (2)$$

In Eq. (2), when the beads i and j are separated by a distance of $r < r_c = 1.5$, a nonlocal bond is formed between them, which lowers the potential energy U_{ij} by an amount $\epsilon_{ij} < 0$ relative to the unbonded energy and stabilizes the overall system in the process. Additionally, all nonlocal monomers interact via a hard-sphere repulsion with a hard-sphere diameter of $r_h = 1.25$ to account for excluded volume interactions at short distances.

A. The crambin model

Crambin is a naturally occurring small protein found in the cabbage seeds of *Crambe abyssinica* consisting of 46 residues. Because of its ability to crystallize easily, an unusual characteristic for a protein, the structure of crambin has been studied using x-ray crystallography^{20–22}. Despite its small size, crambin has various secondary structures: two α -helices, one anti-parallel β -sheet, and three disulfide bridges. In the first α -helix, the bonds span residues 6 to 18; in the second helix, they span residues 22 to 31. In the β -sheet, bonds occur between residues [2, 34] and [3, 33], and the disulfide bridges occur between residues [3, 40], [4, 32], and [16, 26], as given in the Protein Data Bank. Since including many nonlocal bonds in the model is computationally expensive to simulate, we restrict the number of connections in the two α -helices of crambin. Following earlier work¹⁷, interactions are allowed between monomers of indices $i = 2 + 4k$ and $j = i + 4n$, where k is an arbitrary positive integer and $n = 1, 4, 5, \dots$. As a result, crambin's first α -helix is defined by the bonds [6, 10], [10, 14], and [14, 18], and its second helix is defined by the bonds [22, 26], and [26, 33]. Overall, the nonlocal bonds are assumed to occur between beads [2, 34], [3, 33], [3, 40], [4, 32], [6, 10], [10, 14], [14, 18], [16, 26], [22, 26], and [26, 30]. All nonlocal bonds are treated as energetically equivalent, so $\epsilon_{ij} = -\epsilon$, expressed in energy units of $k_B T \equiv \beta^{-1}$. In Fig. 1, the native state of the crambin protein from the Protein Data

Bank and the fully bonded structure of the coarse-grained model are shown.

A recent numerical study of the dynamics of the crambin protein¹⁶ predicted a simple two-step mechanistic folding pathway in the model protein: Helical regions of crambin formed first with no clear preference of order, followed by the passage with near-unit probability through a helical bottleneck state. In the second step, distant bonds linking helix regions to one another lead to a penultimate state with all bonds present except those connecting the most distant edges of the chain. In addition, it was shown¹⁶ that when a diffusive Markov state model is appropriate for the long-time dynamics of the chain, the effect of different choices of the nonlocal bond energies ϵ_{ij} on dynamical properties, such as the mean first passage time from fully extended configurations to the native structure of crambin, may be analyzed to determine optimal state energies for this property. For crambin, it was found that selecting bond energies that decrease the probability of forming early-stage long-range bonds reduces the folding probability pathways through the restrictive bottleneck state and doubles the folding rate relative to the equal bond energy model. In this mechanistic study, which assumed diffusive dynamics, the overall timescale of the folding process was written in a scaled time unit, ℓ^2/D , where D is the self-diffusion coefficient of the nonlocal bonding distances.

In the present work, transitions among macrostates of a single equal bond energy model of a crambin molecule in solution are observed in explicit simulations. Their rates are compared to theoretical predictions based on the diffusive Markov state model.

B. Thermodynamics

In the coarse-grained model, the configurational space of the protein-like chain is partitioned into a set of macrostates, where each macrostate is defined by the bonding pattern or set of satisfied distance constraints. According to the step-potential for bonding contacts, Eq. (2), each nonlocal bond constraint is satisfied or not, depending on whether the pair of nonlocal beads involved are separated by a distance less than r_c . Let the set of positions of the N monomers be given by the set $\mathbf{R} = (r_1, \dots, r_N)$. Since the potential is a square well, the point at which a bond forms or breaks is well-defined, and each nonlocal bond, k , can take on a binary value c_k of value 0 or 1. If $c_k = 0$, the bond is turned off since $x_k > r_c$, where x_k is the distance between the nonlocal beads that form bond k , and if $c_k = 1$, the bond is turned on since $x_k < r_c$. Therefore, the set of nonlocal bonds, n_b , for a particular macrostate c out of a total of $n_s = 2^{n_b}$ macrostates can be represented as a binary string:

$$c = c_1, \dots, c_{n_b}. \quad (3)$$

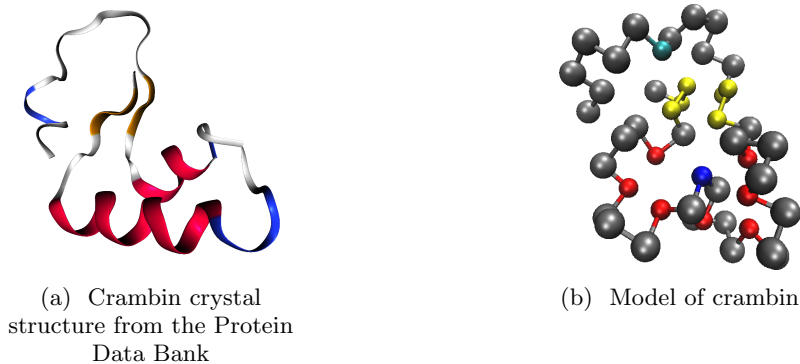


FIG. 1: The model crambin system. Fig. 1a is a cartoon representation of the structure of the crystallized protein. Fig. 1b is the fully-folded minimum entropy state of the 46-bead, ten-bond model. In both figures, the beads participating in nonlocal bonds in the α -helices are in red, the β -sheets are in yellow, and the disulfide bridges are in blue and cyan for beads 16 and 40, respectively.

Defining an indicator function,

$$\mathbb{1}_c(\mathbf{R}) = \begin{cases} 1 & \text{if all constraints for } c \text{ are satisfied,} \\ 0 & \text{otherwise,} \end{cases}$$

the non-ideal configurational entropy of c , a dimensionless value, is given by

$$S_c = \ln \left(\frac{1}{V^N} \int \mathbb{1}_c(\mathbf{R}) d\mathbf{R} \right). \quad (4)$$

The integral over the set \mathbf{R} can be viewed as the volume of the subspace of all possible configurations that satisfy the geometric constraints imposed by the square-well potential and the bonding interactions. As is evident from Eq. (4), S_c is a geometric quantity that depends only on the distance constraints between the beads; hence, models that differ in the specified state energies but have the same bonding interaction distances have the same density of states.

The equilibrium fraction or probability of configuration of c , n_c , is given by the canonical average of the indicator function,

$$n_c = \langle \mathbb{1}_c \rangle = \frac{e^{-\epsilon_c} e^{S_c}}{\sum_{\alpha=1}^{n_s} e^{-\epsilon_\alpha} e^{S_\alpha}} = \frac{e^{-F_c}}{\sum_{\alpha=1}^{n_s} e^{-F_\alpha}},$$

where F_c is the dimensionless free energy of c . Since the configurational entropy is independent of the interaction energy, once S_c has been determined, the probability of configuration c for any choice of interaction energies $\{\epsilon_c|c\}$ (in units of $k_B T$) for the set of states can be evaluated.

C. The Markov state model of dynamics

We assume that each macrostate is long-lived and experiences infrequent but rapid transitions to other macrostates that differ from it by a single bond. The

set of average non-equilibrium populations, $\mathbf{n}(t) = (n_1(t), \dots, n_{n_s}(t))$, defined with respect to an initial distribution, $P(\mathbf{R}, 0)$,

$$n_i(t) = \int d\mathbf{R} P(\mathbf{R}, 0) \mathbb{1}_i(t),$$

evolves according to the Markov state model¹⁸:

$$\frac{d\mathbf{n}(t)}{dt} = \mathbf{K} \cdot \mathbf{n}(t), \quad (5)$$

where \mathbf{K} is the transition rate matrix. If state i is the initial macrostate, with one less bond than state j , the final macrostate, the off-diagonal elements K_{ji} describe a transition between i and j in which an additional bond is formed when the distance r separating the beads reaches r_c . When this bond is formed, the energy is lowered by ϵ . Each matrix element is dependent on the mean equilibrium first passage times, $\tau_{(ij)}^-$ and $\tau_{(ij)}^+$. The inner mean first passage time, $\tau_{(ij)}^-$, is the average time required for two nonlocal beads in state j to diffuse to r_c to reach state i . In state j , r is distributed according to the conditional equilibrium probability density $\rho_{(ij)}^-(r) = n_j^{-1} H(r_c - r) \rho_i(r)$, where $n_j = \int dr H(r_c - r) \rho_i(r)$ is the equilibrium population of state j , $H(r_c - r)$ is a Heaviside function, and $\rho_i(r)$ is the marginal equilibrium density for the distance of the bonding beads when all the bonding constraint conditions in state i are satisfied. Likewise, the outer first passage time, $\tau_{(ij)}^+$, is the average time for nonlocal beads diffusing from a distance $r > r_c$, distributed according to $\rho_{(ij)}^+(r) = n_i^{-1} H(r - r_c) \rho_i(r)$, to reach r_c , thereby yielding a transition from state i to j . By examination of the spectrum of the operator governing the diffusive motion of the system, it can be shown that the inverse of K_{ji} is¹⁸

$$\begin{aligned} K_{ji}^{-1} &= e^{-\epsilon} e^{\Delta S} \tau_{(ij)}^- + \tau_{(ij)}^+ \\ &= \frac{n_i}{n_j} \tau_{(ij)}^- + \tau_{(ij)}^+, \end{aligned} \quad (6)$$

where $\Delta S = S_i - S_j$, and S_i and S_j are the configurational entropies of i and j , respectively. This difference is generally positive for bond-formation events. The elements of the transition matrix obey detailed balance,

$$K_{ji}n_i = K_{ij}n_j, \quad (7)$$

and the probability is conserved such that $\sum_j K_{ji} = 0$. It follows that $K_{ij} = K_{eq}^{-1}K_{ji}$, where $K_{eq} = n_j/n_i$ is the equilibrium constant for the reversible reaction $i \rightleftharpoons j$. The mean first passage times for the i to j transition can be calculated using quadratures¹⁸,

$$\tau_{(ij)}^+ = \frac{1}{D_{(ij)}} \int_{r_c}^{r_{\max}} \frac{(1 - C_{(ij)}^+(r))^2}{\rho_{(ij)}^+(r)} dr = \frac{\bar{\tau}_{(ij)}^+}{D_{(ij)}}, \quad (8)$$

$$\tau_{(ij)}^- = \frac{1}{D_{(ij)}} \int_{r_{\min}}^{r_c} \frac{C_{(ij)}^-(r)^2}{\rho_{(ij)}^-(r)} dr = \frac{\bar{\tau}_{(ij)}^-}{D_{(ij)}}, \quad (9)$$

where r_{\min} and r_{\max} are the minimum and maximum allowed values of the bonding distance that separates two nonlocally bonded beads, and $\bar{\tau}_{(ij)}^\pm$ defines a mean squared diffusion distance with units ℓ^2 . In Eqs. (8) and (9), $D_{(ij)}$ is the diffusion coefficient characterizing the diffusive evolution of the relative bond distance in the absence of the bonding potential, and the cumulative distributions are defined as¹⁸

$$C_{(ij)}^-(r) = \int_{r_{\min}}^r \rho_{(ij)}^-(x) dx,$$

$$C_{(ij)}^+(r) = \int_{r_c}^r \rho_{(ij)}^+(x) dx.$$

In practice, the diffusion coefficients $D_{(ij)}$, which depend on both solvent-bead and local bead-bead interactions, are similar for most pairs of configurations (ij) in the model (see Table II). However, the diffusion coefficients of individual beads depend on the viscosity of the solvent environment in which the protein-like chain is embedded, and this viscosity can differ by many orders of magnitude.

As discussed in the Appendix, the validity of Eq. (6) depends on a number of assumptions: In particular, there must be a separation between the timescale on which contact bonds are formed and broken, leading to a change in the macrostate, and the timescale of the local equilibration of each macrostate. Additionally, the force exerted by the solvent-bead and bead-bead interactions on each bead must be rapid on the timescale of bead motion, and the friction must be strong enough to lead to overdamped bead motion in which velocity correlations decay to zero on a timescale that is shorter than the typical timescale of changes in the positions of the beads.

D. The layer method

Colberg and Schofield¹⁶ developed a layer method in which an adaptive dynamical Monte Carlo scheme was

used to obtain an estimate of S_c in Eq. (4) for each intermediate state as well as to compute numerical estimates of the inner and outer first passage times. The procedure consists of successively evaluating in parallel the entropy difference and first passage times between states that differ by the formation of a single contact using adaptive sampling that combines a Wang-Landau algorithm with a rigorous statistical convergence criterion to establish confidence intervals for all quantities. When a model protein has many possible nonlocal bonds, the number of possible macrostates, n_s , which grows exponentially, is prohibitively large. The large number of states negatively impacts the statistical resolution of adaptive sampling since the set of standard errors of observed quantities decreases¹⁶ at a rate proportional to $n_s^{-1/2}$. The layer method improves the efficiency of the calculation of the density of states by evaluating the differences in entropy of many transitions in parallel while restricting the active set of states to $n_s = 2$.

During each of the sampling iterations for a particular pair of connected macrostates, the distance between the bonding beads in the active bonds is recorded and used to construct analytical fits of the marginal equilibrium probability densities $\rho_{(ij)}^\pm(r)$ and their cumulative distribution, based on a maximum likelihood estimate of the logarithm of the density using splines²³. The mean squared diffusion distances defined in Eqs. (8) and (9) are then obtained by numerical integration of the analytical fits.

E. The diffusion coefficients

In a diffusive Markov state model, all elements of the transition rate matrix \mathbf{K} are proportional to the diffusion coefficient characterizing the evolution of the bonding distance between the relevant nonlocal bond-forming beads. The values of these diffusion coefficients, and hence the timescales of the changes in the macrostates, depend strongly on the nature of the solvent in which the protein-like chain is immersed.

In general, for single mesoscale-sized monomers of large size R and mass M , the self-diffusion coefficient, defined in terms of the time integral of the equilibrium velocity autocorrelation function, can be written as the sum of two components²⁴,

$$D = \frac{1}{3} \int_0^\infty d\tau \langle \mathbf{V}(\tau) \cdot \mathbf{V} \rangle$$

$$= D_0 + D_h, \quad (10)$$

where \mathbf{V} is the velocity of the monomer and D_0 is a bare diffusion coefficient arising from uncorrelated collisions between the monomer and the solvent. In Eq. (10), D_h is a hydrodynamic contribution that accounts for the dynamic correlations induced by the motion of the monomer in the fluid, which is also responsible for the algebraic decay of the velocity autocorrelation function (VACF) on

hydrodynamic timescales^{25,26}. For a spherical monomer in a hard-sphere fluid, the bare diffusion coefficient, D_0 , arising from the rapid loss of velocity correlations due to solvent collisions on molecular timescales, is approximately given by the Enskog result^{24,27},

$$\begin{aligned} D_0 &= \frac{k_B T}{\chi_0}, \\ \chi_0 &= \frac{8\rho}{3} R^2 g(R) \sqrt{2\mu_m \pi k_B T}, \end{aligned} \quad (11)$$

where k_B is Boltzmann's constant, T is the temperature of the system, ρ is the number density of the solvent, m is the mass of a solvent particle, $\mu_m = Mm/(M+m)$ is the reduced mass, and $g(R)$ is the radial distribution function at contact²⁸. Asymptotically, when the size of the monomer R is much larger than the correlation length ξ induced by the solvent-monomer interaction potential (i.e. the boundary layer)²⁶, an approximate form of the hydrodynamic contribution for an unbounded system is given by the Stokes' result in the slip limit^{29,30},

$$\begin{aligned} D_h &= \frac{k_B T}{\chi_h}, \\ \chi_h &= 4\pi\eta_d R, \end{aligned} \quad (12)$$

where η_d is the dynamic viscosity and R is the hydrodynamic radius. For large Brownian particles, such as in the case of a large sphere suspended in a hard-sphere fluid, $D_h \gg D_0$, since D_0 and D_h scale differently with R , the hydrodynamic size of the monomer. The clear separation between molecular scale and hydrodynamic contributions to diffusion breaks down as the size of the monomer approaches the thickness of the boundary layer, $R \sim \xi$. Furthermore, for finite systems, such as those in computer simulations, important correction terms to the hydrodynamic friction χ_h arise from the long-ranged nature of the hydrodynamic interactions³¹.

The derivation of microscopic expressions for the diffusion coefficient $D_{(ij)}$ for the relative bond distance in the protein-like chain is complicated by the contribution of the local bead-bead interactions to the non-hydrodynamic friction, χ_0 . The collisions of a monomer with its local nearest and next-nearest neighbors can occur on a timescale that is not clearly separated from the timescale of collisions between the monomer and the solvent, resulting in negative velocity correlations and a reduction in the self-diffusion coefficient as observed in dense fluids in which caging is prominent. The local interactions typically result in a $D_{(ij)}$ that differs significantly from the case in which monomers are not connected in a chain, in which case $D_{(ij)} = 2D_0$. In the absence of theoretical results for such systems, the bond distance diffusion coefficients must be evaluated by direct numerical simulation.

III. MODELS OF THE SOLVENT BATH

The modeling of a solvent bath faces the same challenges as simulating the chain itself. Atomistic calculations are computationally expensive, and the microscopic timescales of the monomer motions are orders of magnitude shorter than the timescale on which conformational changes occur in biological systems³². Coarse-graining can recreate the behavior of an atomistic system at timescales that more closely resemble biological systems. Some coarse-grained approaches, such as a continuum model based on the Stokes equation³², are too simplistic since they implicitly omit important physical effects such as thermal fluctuations, which play an important role in the motion of the solvent and small solutes. We will use three models of the solvent of decreasing complexity that progressively simplify physical phenomena: A hard-sphere model, a multi-particle collision model that neglects fluid structure, and, finally, a penetrating solvent model in which an effective fluid is simulated through stochastic collisions that periodically modify the bead velocities while neglecting hydrodynamic interactions.

A. The hard-sphere solvent model

In a hard-sphere model, the treatment of the solvent particles is similar to that of the beads in a protein-like chain: Each particle is represented by a hard-sphere, which travels in a straight line until it experiences an elastic collision due to an encounter with another particle. As a result, hydrodynamic flow and solvent-solvent interactions are present in the hard-sphere model. Since the hard-sphere solvent particles occupy a non-zero volume, unlike point particles, the physical configurations of the solvent require non-overlapping solvent spheres.

Theoretical predictions for the self-diffusion coefficient of a large and massive monomer in a hard-sphere fluid can be obtained from kinetic theory²⁹. Accurate expressions³³ of the radial distribution function at contact, $g(R)$, can be used in the Enskog expression in Eq. (11) to evaluate the bare diffusion coefficient D_0 , and the hydrodynamic contribution to the self-diffusion coefficient of the monomer, D_h , can be estimated using Enskog results for the dynamic viscosity²⁷. The predicted forms of the self-diffusion coefficient in a hard-sphere fluid are useful to determine the physical conditions, such as the particle size and number density, which are required for modeling fluids with specified physical characteristics.

B. The multi-particle collision dynamics solvent model

MPCD, also known as stochastic rotation dynamics (SRD), is a solvent model developed by Malevanets and Kapral in which the solvent is coarse-grained to eliminate the calculation of solvent-solvent interactions^{32,34-36}.

Therefore, intermolecular interaction potentials between solvent particles and structural ordering in the fluid cannot occur³⁷. MPCD is carried out in two alternating steps: a solvent streaming step, in which solvent particles move in the presence of the solute, and a stochastic solvent collision step. In this model, the solvent's mass, momentum, and energy are conserved locally, resulting in dynamics consistent with hydrodynamic flow. Due to the conservation of energy, MPCD can be used for simulating microcanonical ensembles³². Both hydrodynamic flow and thermal fluctuations are included in this model, but the collisions between the solvent particles are carried out at specific steps rather than continuously throughout the simulation.

In the hard-sphere MPCD model, the solvent consists of a large number N_s of particles, each with mass m ^{32,36}. These particles move independently and interact with the monomers of the solvated chain via elastic collisions. Solvent-solvent interactions occur via collision steps at discrete time intervals, Δt , which, unlike the time intervals in molecular dynamics, do not need to be small³². Let the volume occupied by the system of solvent particles be divided into a grid made up of N_x cubic cells, each with side length a ^{32,36}. Within each cell ϕ , there are N_ϕ solvent particles. Each particle can only interact with its cell mates and not with the particles in neighboring cells. The particles can also cross from one cell to another; thus, the quantity $N_\phi(t)$ is dynamic. The cells have a center of mass velocity, $\mathbf{V}_\phi(t)$, where

$$\mathbf{V}_\phi(t) = \frac{1}{N_\phi(t)} \sum_{j=1}^{N_\phi(t)} \mathbf{v}_j(t), \quad (13)$$

where each particle j in the set of $N_\phi(t)$ particles is positioned in cell ϕ at the rotation time.

The post-collision velocity at collision time t , $\mathbf{v}'_i(t)$, of particle i located in a cell ϕ with center of mass velocity $\mathbf{V}_\phi(t)$, is given by

$$\mathbf{v}'_i(t) = \mathbf{V}_\phi(t) + \hat{\omega}_\phi \cdot (\mathbf{v}_i(t) - \mathbf{V}_\phi(t)), \quad (14)$$

where $\hat{\omega}_\phi$ is a rotation operator assigned to cell ϕ chosen randomly from a set of rotation operators, Ω ^{32,36}. Therefore, the relative particle velocities within a given cell undergo the same rotation, while the rotation matrices $\hat{\omega}_\phi$ for each cell differ. There are several ways in which a rotation can be carried out. Here, the particle velocities in each cell are rotated by an angle α about a randomly chosen direction $\hat{\mathbf{u}}$. Therefore, the post-collision velocity of i in a cell ϕ can be rewritten as

$$\begin{aligned} \mathbf{v}'_i(t) &= \mathbf{V}_\phi(t) + \hat{\mathbf{u}} \hat{\mathbf{u}} \cdot (\mathbf{v}_i(t) - \mathbf{V}_\phi(t)) \\ &\quad + (\mathbf{I} - \hat{\mathbf{u}} \hat{\mathbf{u}}) \cdot (\mathbf{v}_i(t) - \mathbf{V}_\phi(t)) \cos \alpha \\ &\quad - \hat{\mathbf{u}} \times (\mathbf{v}_i(t) - \mathbf{V}_\phi(t)) \sin \alpha. \end{aligned} \quad (15)$$

Finally, prior to the collision step, the entire cell grid is shifted by a uniform random displacement vector to preserve Galilean invariance^{32,38,39}.

For an MPCD fluid in which fluid particles interact with the monomer beads by a hard-sphere potential, the bare diffusion coefficient D_0 for a single monomer is given by Eq. (11) with $g(R) = 1$. The hydrodynamic contribution D_h can be approximated using the explicit form for the dynamic viscosity, $\eta_d = m\rho(\eta_k + \eta_c)$, where η_k and η_c are the kinetic and collisional contributions to the viscosity³² given by

$$\begin{aligned} \eta_k &= \left[\frac{5N_c}{(N_c - 1 + e^{-N_c}) [2 - \cos(\alpha) - \cos(2\alpha)]} - 1 \right] \frac{k_B T \Delta t}{2m} \\ \eta_c &= \left[\frac{(N_c - 1 + e^{-N_c})}{18N_c} [1 - \cos(\alpha)] \right] \frac{a^2}{\Delta t}, \end{aligned} \quad (16)$$

and $N_c = \rho a^3$ is the average number of particles in one cubic cell.

C. The penetrating solvent model

In the penetrating solvent model, the solvent interactions are implicitly included by creating fictitious solvent-bead collisions^{32,37}. The interactions between solvent particles and monomers occur through rotations of the monomer velocities relative to an effective center of mass velocity,

$$\mathbf{V}_\phi(t) = \frac{M}{M_t} \mathbf{v}_i(t) + \frac{N_s m_s}{M_t} \mathbf{v}_s(t), \quad (17)$$

where N_s is randomly chosen from a Poisson distribution with a mean of $N_c = \rho V_{\text{cell}} = \rho a^3$. In Eq. (17), $M_t = M + N_s m$, and \mathbf{v}_s is chosen from a normal distribution with a zero mean and a variance of $k_B T / (N_s m_s)$, where T is the system's temperature. Post-collision, the velocity of the bead is given by Eq. (15).

Unlike the previous two models, there is no hydrodynamic contribution, D_h , to the diffusion coefficient of the penetrating solvent model as there is no fluid velocity field. Rather, the value of $D = D_0$ arises purely from the uncorrelated collisions between the fictitious solvent and bead particles. By explicitly calculating the VACF and its integral, one finds³⁷:

$$D = \frac{k_B T}{M} \Delta t \left(\frac{2 - \gamma}{2\gamma} \right), \quad (18)$$

where γ is given by

$$\gamma = \frac{2N_c}{3(1 + \mu)} M(1, 2 + \mu, -N_c), \quad (19)$$

and $M(1, 2 + \mu, -N_c)$ is Kummer's function of the first kind⁴⁰. Here, $\mu = M/m$ is the ratio of the bead and solvent masses.

IV. PARAMETERIZATION OF SIMULATIONS

To compare the population equilibration rate for model proteins immersed in the hard-sphere, MPCD, and penetrating solvent models, the simulation parameters must

be chosen such that monomer dynamics are similar in the three models. To select these parameters, a massive (Brownian) bead in equilibrium with the solvent was simulated in the respective solvent models. Each parameter was designed to yield closely matched velocity autocorrelation functions and diffusion coefficients. In addition, the mean-squared displacements (MSD) of the Brownian bead, $\langle |\mathbf{X}(t) - \mathbf{X}(0)|^2 \rangle$, were monitored. All particles were confined to a cubical box of side length L with periodic boundary conditions in all directions. For the penetrating and MPCD models, $L = 10\ell$, where ℓ is the simulation unit of length, whereas for the hard-sphere model, $L = 9\ell$. The slightly smaller box size for the latter model was chosen to reduce the number of hard-sphere solvent particles needed due to the high computational cost of simulating the monomer-solvent and solvent-solvent collisions. In the penetrating and MPCD models, the number density was $\rho = 8.87\ell^{-3}$, and in the hard-sphere model, the number density was $\rho = 10\ell^{-3}$. For all models, the mass M of the Brownian particle was set to be six times the mass of the solvent particles m , taken to be the unit of mass since an amino acid weighs, on average, six times more than a water molecule. The rotation time Δt was taken to be 0.25τ for the penetrating solvent model, while for the MPCD model, it was $\Delta t = 0.5\tau$, where $\tau = \sqrt{m\ell^2/(k_B T)}$ is the simulation time unit. In both cases, the rotation angle was $\alpha = 90^\circ$. The radius of the Brownian particle was 0.5ℓ for the penetrating and MPCD models, whereas for the hard-sphere model, it was 0.4ℓ . In the MPCD solvent, the cell length $a = \ell$. The radius of each hard-sphere solvent particle was set to 0.1ℓ , since water molecules are approximately three to four times smaller than an amino acid. As a result of the choice of these parameters, the mean free path for the MPCD model was $\lambda = \Delta t/\tau \cdot \sqrt{k_B T/m} = 0.5\ell$. For these parameters, $\chi_h/\chi_0 \sim b\ell/(Rg(R))[(5\Delta t)/(4\tau) + \tau/(9\Delta t)] \sim 4.77$, where $b = 18\pi/\sqrt{32\pi}$, so the hydrodynamic contribution D_h to the diffusion coefficient of a single bead is expected to be smaller than the direct interaction contribution, D_0 . For larger values of R/ℓ , the hydrodynamic contribution D_h dominates D_0 . Using these parameters, the resulting unnormalized VACF curves from all three solvent models, the integral of which defines the self-diffusion coefficient according to Eq. (10), were found to be nearly identical when overlaid, as can be seen in Fig. 2.

The parameters prescribed earlier were used in equilibrium simulations to obtain diffusion coefficients for all three solvent models. For the Brownian system, the diffusion coefficient was evaluated in two ways: by computing the running integral of the VACF, and by a least squares polynomial fit of the short, linear portion of the mean squared displacement (MSD). The two expressions for the diffusion coefficient are related by noting that for

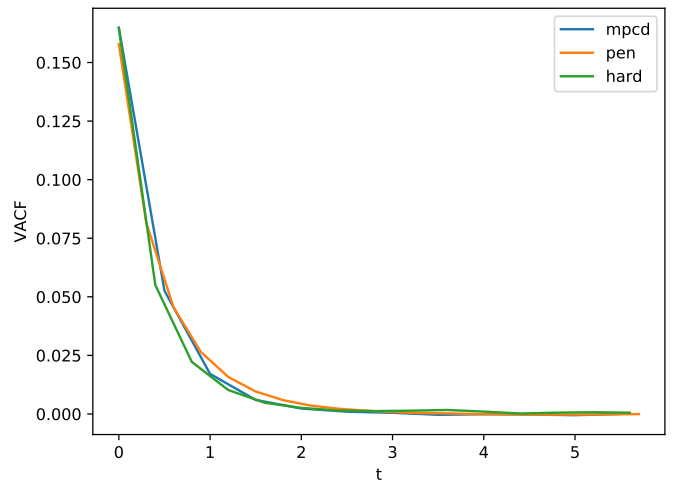


FIG. 2: Unnormalized velocity autocorrelation curves $\langle \mathbf{V}(t) \cdot \mathbf{V} \rangle / 3$ vs. time (in simulation units τ) for a Brownian particle diffusing in a bath.

Solvent model	D_{MSD}	D_{VACF}
Penetrating	0.080	0.085
MPCD	0.074	0.079
Hard-sphere	0.073	0.080

TABLE I: Diffusion coefficients in units of ℓ^2/τ of the Brownian system immersed in the penetrating, MPCD, and hard-sphere solvent models.

$t \gg \tau$, the MSD satisfies

$$\begin{aligned} \langle |\mathbf{X}(t) - \mathbf{X}(0)|^2 \rangle &= 2t \int_0^t d\tau (1 - \tau/t) \langle \mathbf{V}(\tau) \cdot \mathbf{V}(0) \rangle \\ &\approx 6D(t)t, \end{aligned} \quad (20)$$

where

$$D(t) = \frac{1}{3} \int_0^t d\tau \langle \mathbf{V}(\tau) \cdot \mathbf{V} \rangle. \quad (21)$$

The diffusion coefficient estimates for each solvent model are recorded in Table I.

The typical value of the diffusion coefficient was found to be $D = 0.08 \ell^2/\tau$, in simulation units. Appropriate length, mass, and energy scales must be identified to compare this diffusion coefficient value for a Brownian monomer to experimental values. Theoretical estimates of the diffusion coefficient in protein systems typically rely on the Stokes-Einstein law (i.e. Eq. (12)), which requires the input of the effective spherical hydrodynamic radius and the viscosity of the solvent⁴¹. For monomers or groups of atoms *within* a protein, neither the choice of the effective hydrodynamic radius R nor the local viscosity of the monomer in the fluid is apparent. Experiments generally measure the protein's mass diffusion center rather than the diffusion coefficient of monomers or groups of atoms, and typical values of $5 \cdot 10^{-10} \text{ m}^2/\text{s}$ are

found^{42,43}. The length scale ℓ is set to the average length of a covalent bond between two amino acids¹⁷, $\ell = 3.84$ Å, and estimating the average solvent mass m in the cytoplasm to be on the order of 100 amu, $\tau = 2.27 \cdot 10^{-12}$ s and $D \approx 5 \cdot 10^{-9}$ m²/s in standard units. This value of the diffusion coefficient is roughly ten times larger than estimates of the diffusion coefficient of the center of mass of large substrates^{37,41–44}. In dilute solutions⁴⁵, the center of mass self-diffusion coefficient of a polymer scales with the number of monomers N as $N^{-0.55}$, so the monomer diffusion measured in the simulation would correspond to a small protein of roughly 65 monomers, roughly the size of the crambin protein. For the penetrating and MPCD fluid models, the monomer diffusion coefficients can be reduced by decreasing the rotation time Δt , hence increasing the frequency of stochastic rotations, with a proportional increase in the computational burden of simulating the solvated system. Increasing the number density of hard-sphere fluid particles similarly leads to a roughly proportional increase in the bare and hydrodynamic friction, χ_0 and χ_h , respectively, while increasing the computational burden at least quadratically.

V. SIMULATED DYNAMICS

To verify the diffusive Markov state model of the dynamics for the different solvents, we consider the dynamics of a single layer in which a single transient bond is allowed to form and break to allow transitions between the unbonded state u and the bonded state b . Denoting the relative equilibrium population of the unbonded state as $n_u^{\text{eq}} = n_u / (n_u + n_b)$ and its instantaneous population as $n_u(t)$, the two-state Markovian dynamics for the population difference, $\delta n_u(t) = n_u(t) - n_u^{\text{eq}}$, and instantaneous population, $n_u(t)$, are given by

$$\begin{aligned} \delta n_u(t) &= e^{-(K_{bu} + K_{ub})t} \delta n_u(0) = e^{-k_r t} \delta n_u(0), \\ n_u(t) &= n_u^{\text{eq}} + (n_u(0) - n_u^{\text{eq}}) e^{-k_r t}, \end{aligned} \quad (22)$$

where the decay rate k_r from an initial non-equilibrium population difference $\delta n_u(0)$ is $k_r = K_{bu} + K_{ub} = K_{bu}(1 + K_{\text{eq}}^{-1})$.

Fig. (3) shows a typical relaxation profile of an ensemble of particles with a mass ratio $M/m = \mu = 20$, initially distributed in an unbonded equilibrium state for an analytically solvable model in which each particle moves freely and independently in a penetrating solvent (described in Sec. III C), and experiences a discontinuous drop in potential energy of $\epsilon = 1$ at a radial distance $R = 1$ from the origin inside a sphere with a reflecting boundary at $R = 2$. As is evident in Fig. (3), although the relaxation profile is expected to deviate from a single exponential for a diffusive process, most notably at short times, the overall timescale of relaxation is well-described by a single exponential of relaxation time k_r^{-1} . As discussed in the Appendix, if desired, the predicted profile can be improved by a higher-order Padé approximation

that includes the initial rate of decay of the populations and its integrated first moment.

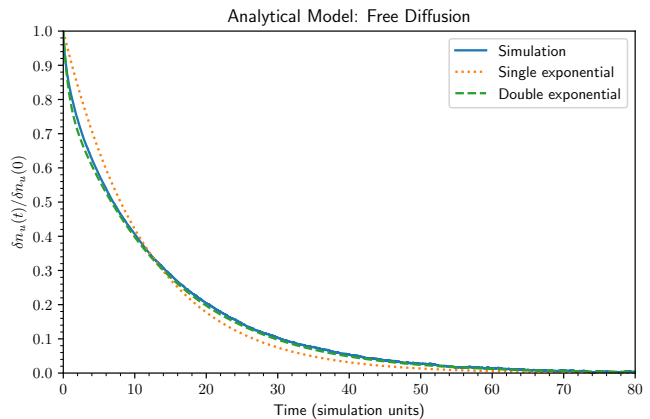


FIG. 3: A relaxation profile for an ensemble of $N_e = 10^5$ initially unbonded free particles (state u) with a mass ratio of $\mu = 20$ and diffusion coefficient $D = 0.0205 \ell^2 / \tau$, corresponding to a rotation time $\Delta t = 0.005 \tau$, in an implicit solvent of number density $\rho = 10 \ell^{-3}$. A reflecting boundary at $R = 2$ confines the particles, and the particles experience a discontinuous drop in the potential of $\epsilon = k_B T$ at $R = 1$. The solid line is the simulation result, the dotted lines are analytical predictions for the decay using Eq. (6), and the dashed lines are a higher-order Padé approximation to $\delta n_u(t) / \delta n_u(0)$, as discussed in the Appendix.

The coarse-grained model of crambin has $n_b = 10$ bonds, which gives $n_s = 1024$ possible macrostates. There are a total of 5120 possible transitions and, therefore, individual simulations. While simulating the entire set of transitions may be feasible in some cases, it is computationally expensive to do for all but the simplest models with a solvent present. As a result, in this work, ten representative transitions for crambin were chosen, each from a different layer, corresponding to a different number and set of permanently maintained bonds. The position of the active bond in each transition is also different. The selected transitions include qualitatively different transition elements: In each higher layer, the initial state was chosen to have different bonding patterns from the pattern studied in the lower layers (with fewer nonlocal bond constraints). The layer number, initial and final bit patterns of the intermediate states in these transitions, the difference in entropy between the respective states, and the inner and outer first passage times computed using the layer method as described in Sec. IID are given in Table II.

A. The bond distance diffusion coefficient

To evaluate the diffusion coefficients, $D_{(ij)}$, for the bonding distances that are critical to identifying the

Layer	Initial State	Final State	ΔS	$\bar{\tau}_{(ij)}^-$	$\bar{\tau}_{(ij)}^+$	$D_{(ij)}$
0	000000000	000000001	3.68	0.0170	3.1	0.0403
1	100000000	100001000	3.56	0.0173	2.9	0.0400
2	0000100100	0000100110	3.24	0.0172	2.0	0.0308
3	1000000110	1010000110	6.97	0.0146	82	0.046
4	0100101100	1100101100	3.92	0.0151	3.1	0.0394
5	0011110010	0011110110	5.82	0.0138	21	0.0362
6	0011111010	0111111010	3.69	0.0148	2.4	0.027
7	0110110111	0111110111	3.07	0.0163	1.54	0.027
8	1111001111	1111101111	3.25	0.0179	2.3	0.0358
9	1111101111	1111111111	3.82	0.0160	3.1	0.027

TABLE II: The layer number and bit patterns of crambin’s initial and final states simulated in the presence of a solvent. The bits indicate which bonds are formed in the respective states in the 46 bead protein model according to Eq. (3), where the indexing refers to the set of ten bonds: [2, 34], [3, 33], [3, 40], [4, 32], [6, 10], [10, 14], [14, 18], [16, 26], [22, 26], and [26, 30]. The percent error for ΔS is less than 5%; for $\bar{\tau}_{(ij)}^-$ and $\bar{\tau}_{(ij)}^+$, it is 5%; and for $D_{(ij)}$, it ranges from 1% to 6%. The diffusion coefficients $D_{(ij)}$ are the simulation results for the penetrating solvent model.

timescale of structural transitions in the Markov state model, simulations for each of the layers of crambin given in Table II were run with $\epsilon = 0.0$ for each type of solvent. To compute $D_{(ij)}$, the positions of the two beads in the active bond were recorded at regular time intervals, and the MSD was calculated. As with the Brownian particle, a least squares polynomial fit was performed over a linear portion of the MSD data. This was done at intermediate timescales $\tau_i \sim 2\tau \ll k_r^{-1}$ that were longer than the ballistic timescale but shorter than the timescale of bond formation. From this fit, the diffusion coefficient was obtained and used to predict the values of the Markov state model rates k_r and the equilibrium population n_u^{eq} for the chosen transitions.

In the absence of all local bonding interactions that contribute an internal source of friction, we expect that $D_{(ij)} \approx 2D_0$, where $D_0 \sim 0.08\ell^2/\tau$, is the diffusion coefficient for a single monomer. From the values in Table II, it is evident that the configurationally-dependent local interactions produce internal friction that significantly reduces the bond distance diffusion coefficient, and $D_{(ij)}$ tends to smaller values at higher layers where more permanent bonds restrict the motion along the bond formation coordinate.

B. Analysis of simulations

To obtain numerical estimates for the k_r and n_u^{eq} for transitions between crambin macrostates, simulations were carried out for all layers in Table II at three values of ϵ : 3.0, 4.0, and 5.0. These values of ϵ yielded a good balance of sufficiently accurate data and fast simulation

times.

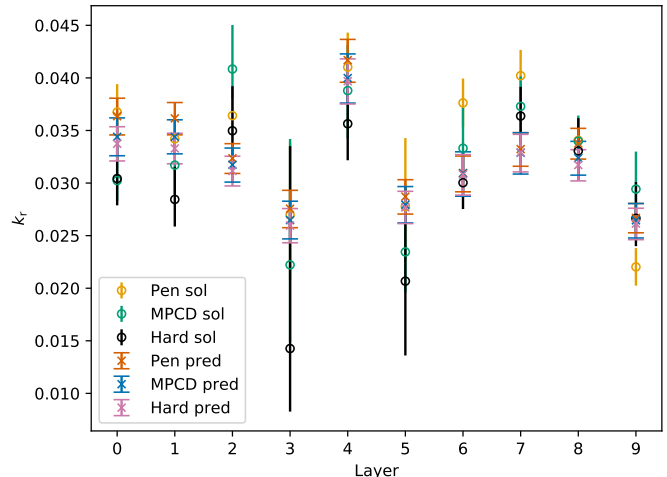


FIG. 4: The k_r for crambin for all three solvent models at $\epsilon = 3.0$. In the legend, the keywords *pen sol*, *mpcd sol*, and *hard sol* correspond to the k_r values from the penetrating, MPCD, and hard-sphere solvent models respectively, and *pen pred*, *mpcd pred*, and *hard pred* represent the rates predicted using the diffusive Markov state model.

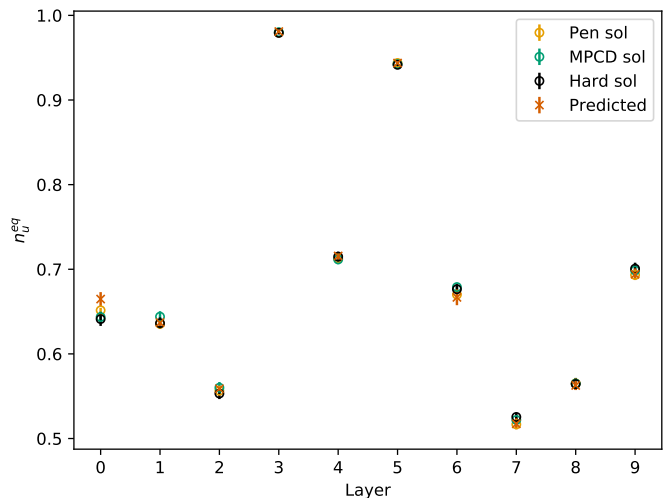


FIG. 5: The n_u^{eq} for crambin for all three solvent models at $\epsilon = 3.0$.

Throughout each simulation, the fraction of the ensemble in the unbound state, an estimator of the probability $n_u(t)$, was recorded at regular time intervals. These data were then fit to an exponential of the form in Eq. (22), using a non-linear least squares procedure. From this fit, the values of k_r and n_u^{eq} were obtained. Both the analytical predictions and simulation results for the hard-sphere, MPCD, and penetrating solvent models are plotted in Figs. 4 and 5. The error bars in these figures, and in Figs. 10, 11, and 12, were obtained using bootstrap sampling of ensemble member trajectories⁴⁶. The number of

bootstraps used for each pair of error bars was 300, and the size of each bootstrap sample was equivalent to the size of the overall ensemble, N_e , typically larger than 10^5 . For every set of bootstrap samples, the observed quantities, namely the rates k_r , the equilibrium populations n_u^{eq} , as well as the bond distance coefficient $D_{(ij)}$, were evaluated and used to establish 95% confidence intervals. To do so, the observed values were ordered from smallest to largest, and the upper and lower confidence limits were the values at the 2.5% and 97.5% percentiles, respectively. This procedure was carried out since the data from the bootstraps were typically not normally distributed.

For the diffusive Markov model of crambin, the predicted values of the equilibrium probability n_u^{eq} and the decay rate $k_r(\epsilon)$ for a bond energy ϵ are given by

$$n_u^{\text{eq}} = \frac{e^{-\epsilon} e^{\Delta S}}{1 + e^{-\epsilon} e^{\Delta S}}, \quad (23)$$

$$k_r(\epsilon) = \frac{D_{(ij)} (1 + e^{-\epsilon} e^{\Delta S})}{\bar{\tau}_{(ij)}^+ + e^{-\epsilon} e^{\Delta S} \bar{\tau}_{(ij)}^-}. \quad (24)$$

The confidence intervals for these predicted values depend on the statistical errors of $D_{(ij)}$, ΔS , and the mean first passage times. The error in ΔS was obtained by running the dynamics of the same transition ten times and finding the relative error across these results. The relative error of the mean first passage times was obtained in the same way and was found to be 5% of the value of each mean first passage time or less in Ref. 16, so for simplicity, here we set the relative error to 5%. This led to the total error for the predicted k_r and state probability n_u^{eq} being that indicated by the error bars in the figures provided in the following section.

Since the solvent is in thermal equilibrium with the protein chain and the instantaneous interaction solvent-monomer energies are always zero for all solvent models considered here, the presence of the solvent does not influence the equilibrium population of the unbound state n_u^{eq} . Hence, the dynamics of the population of the unbound state for all solvent models must tend to the same value, n_u^{eq} , a result confirmed in Fig. 5.

VI. RESULTS

Of the ten transitions occurring between the intermediate states of crambin listed in Table II, two representative layers with qualitatively different characteristics containing three and eight permanent bonds (see Fig. 6), respectively, showcase the analysis of the simulation data.

The detailed results for these layers are presented in Fig. 7. In layer 8, the active bond is a fast-forming, short-range α -helix bond occurring between beads [6, 10], whose configurational entropy difference was the second smallest of the ten layers. In addition, the outer squared diffusion distance is short ($\bar{\tau}_{(ij)}^+ = 2.3 \ell^2$). In contrast, the active bond in layer 3 is a slow-forming, long-range disulfide bridge between beads [3, 40], with a large mean

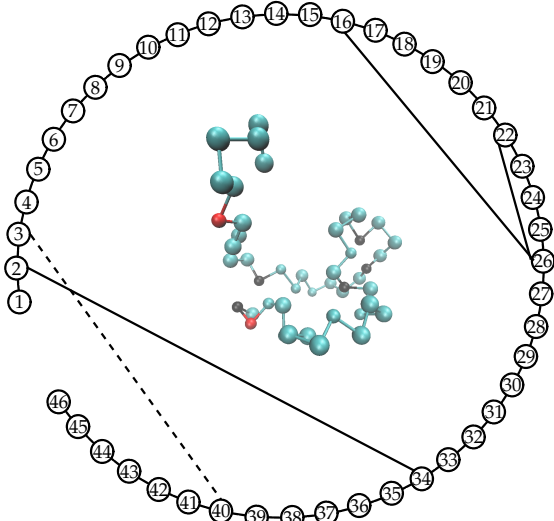
Layer	n_u^{eq}	k_r
3 (sol)	$0.9796 \pm 5\text{e-}4$	$0.027 \pm 6\text{e-}3$
3 (MSM)	$0.9808 \pm 7\text{e-}4$	$0.028 \pm 2\text{e-}3$
8 (sol)	$0.565 \pm 3\text{e-}3$	$0.034 \pm 2\text{e-}3$
8 (MSM)	$0.563 \pm 5\text{e-}3$	$0.034 \pm 1\text{e-}3$

TABLE III: n_u^{eq} and k_r for layers 3 and 8 for the penetrating solvent and diffusive Markov state models at $\epsilon = 3.0$.

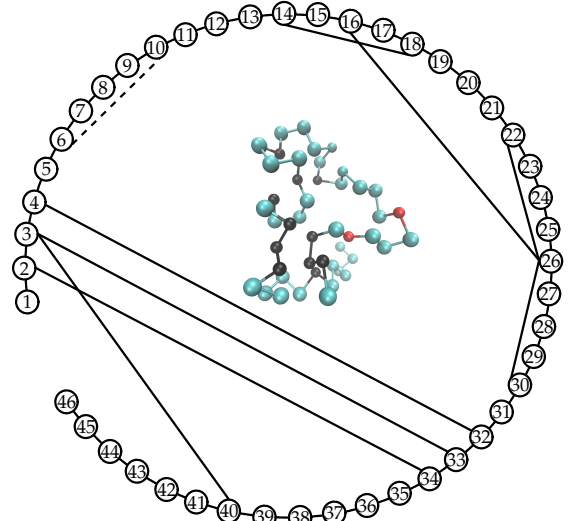
first passage time (since $\bar{\tau}_{(ij)}^+ = 82 \ell^2$) approximately 40 times larger than that of layer 8. The configurational entropy difference $\Delta S = 6.97$ of this bond, which is strongly correlated with the outer mean first passage time, is more than twice as large as that of layer 8.

Looking at Fig. 7 and Table III, it is clear that while the equilibration rates k_r for the two layers are similar, the equilibrium populations n_u^{eq} as well as the outer first passage times are quite different. The value of n_u^{eq} of layer 3 is much larger than that of layer 8, since the entropic cost of forming the disulfide bond between the distant monomer pair [3, 40] is high, even though a β -sheet link between the monomer pair [2, 34] already exists. In comparison, the entropic cost of forming the local helical bond [6, 10] in layer 8, which decreases the potential energy of the molecule by the same factor of $\epsilon = 3.0$, is lower ($\Delta S = 3.25$) since beads 6 and 10 are restricted to being near one another by the eight other bonds already formed. The same trend is seen across all other layers (see Fig. 5). In layer 5, the value of n_u^{eq} is large because the bridge bond being formed between beads [16, 26] is relatively long-range (accordingly, the configurational entropy difference is large: a value approximately twice that of layer 8). Interestingly, we do not see this trend occurring in layers 4 and 7, despite the active bonds in these layers being the β -sheet bond between [2, 34] in the former and the bridge bond between [4, 32] in the latter. The configurational entropy difference is small as well: the value for layer 8 is approximately equivalent to layer 7 and three-fourths the magnitude of layer 4. This is because in the unbound state, at least one long-range bond has been formed, bringing the opposite ends of the protein together, making the formation of subsequent long-range bonds in this region less entropically costly. In the case of layers 4 and 7, the β -sheet bond between the beads [3, 33] has already been formed, facilitating the formation of future disulfide bridges and β -sheet bonds in the vicinity of these two beads.

Another difference between layers 3 and 8 in Fig. 7 is the magnitude of the fluctuations of the populations relative to the change in the populations, $\delta n_u(0) = 1 - n_u^{\text{eq}} = n_b^{\text{eq}}$, of the unbound state from the initial population of unity. When the equilibrium-bound population n_b^{eq} is small, larger ensembles are required to resolve the relative population decay, $\delta n_u(t)/\delta n_u(0)$, since the statistical uncertainty in the population with an ensemble size



(a) The bonding pattern for transition 1000000110 to 1010000110 in layer 3



(b) The bonding pattern for transition 1111001111 to 1111101111 in layer 8

FIG. 6: The bonding pattern for crambin in the transitions in layers 3 and 8 represented as a linear chain, with the permanently maintained bonds shown as a solid link and the active bond as a dotted link. In the ball and stick models in the centers, the black beads are involved in permanent bonds, while the red beads are the transient bond beads.

of N_e relative to $\delta n_u(0)$ is $\sigma_E/n_b^{\text{eq}} = (n_u^{\text{eq}}/(N_e n_b^{\text{eq}}))^{1/2}$ when the populations are Bernoulli distributed. Since the value of n_b^{eq} increases with the depth of the bonding well ϵ , the statistical errors decrease for larger values of ϵ , and smaller ensembles can be used, as is apparent in Fig. 8. The consideration of the relative magnitude of fluctuations is important for computationally intensive solvent models such as the hard-sphere model. The poor statistical resolution of the values of k_r and n_u^{eq} for layer 3 for the hard-sphere solvent in Figs. 4 and 5 is a direct consequence of the limitations of the small effective ensemble size $N_e n_b^{\text{eq}}$ for this system. This interpretation is confirmed by noting that an increase in the value of ϵ noticeably reduces the relative fluctuations, a consideration that is important for more detailed and computationally expensive solvent models where the ensemble size N_e is limited (see Fig. 8).

The ratios between k_r at different ϵ were calculated for all three solvent models, and these are presented in Figs. 10 and 11. The rate ratios are computed as

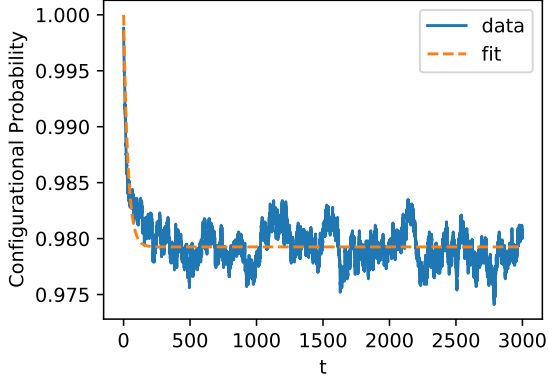
$$\begin{aligned} \frac{k_r(\epsilon_1)}{k_r(\epsilon_0)} &= \left(\frac{1 + e^{-\epsilon_1} e^{\Delta S}}{1 + e^{-\epsilon_0} e^{\Delta S}} \right) \frac{\bar{\tau}_{(ij)}^+ + e^{-\epsilon_0} e^{\Delta S} \bar{\tau}_{(ij)}^-}{\bar{\tau}_{(ij)}^+ + e^{-\epsilon_1} e^{\Delta S} \bar{\tau}_{(ij)}^-} \\ &= \left(\frac{n_b^{\text{eq}}(\epsilon_0)}{n_b^{\text{eq}}(\epsilon_1)} \right) \frac{\bar{\tau}_{(ij)}^+ + e^{-\epsilon_0} e^{\Delta S} \bar{\tau}_{(ij)}^-}{\bar{\tau}_{(ij)}^+ + e^{-\epsilon_1} e^{\Delta S} \bar{\tau}_{(ij)}^-}. \end{aligned} \quad (25)$$

Although the overall timescale of the relaxation rates k_r is determined primarily by the self-diffusion coefficients $D_{(ij)}$, the rates of the different layers also depend on the outer squared diffusion distance $\bar{\tau}_{(ij)}^+$. For large values

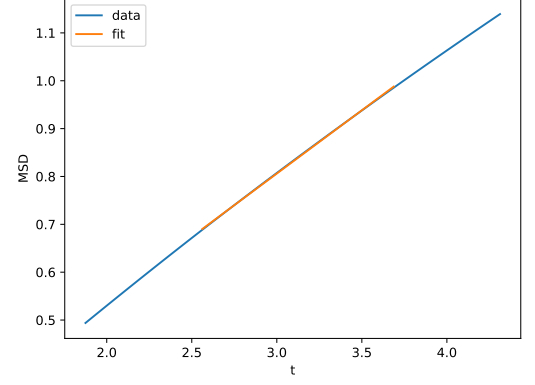
of ϵ relative to the entropic difference ΔS , k_r is inversely proportional to $\bar{\tau}_{(ij)}^+$, a quantity that can be computed without explicitly simulating the dynamics. By examining the ratio of rates at different values of ϵ , the statistical errors introduced by measuring the diffusion coefficients can be bypassed, and the validity of the diffusive Markov state model can be tested without reference to any dynamical quantities related to time correlation functions.

Once again, the trend for the rate ratios predicted by Eq. (25) is borne out in the simulations for all solvents. Since the ratio of the mean first passage time contributions to the rate ratio is close to unity due to the fact that $\bar{\tau}_{(ij)}^+ \gg \bar{\tau}_{(ij)}^-$, the ratio of the bound populations primarily determines the change in rates as a function of the well depth. The largest drop in the equilibration rate occurs for layers 3 and 5, where the ratio of the populations, $n_b^{\text{eq}}(3)/n_b^{\text{eq}}(5) \ll 1$, decreases the most as ϵ increases. These results confirm the importance of the equilibrium populations in the dynamics, which are determined entirely by the geometric constraints, a non-trivial result implied by the diffusive Markov state model.

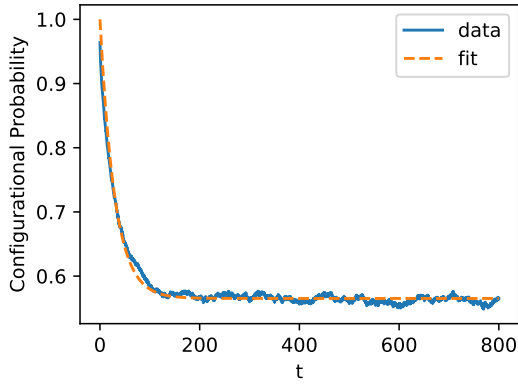
The simulation results described earlier apply to relatively dilute solvents with larger bond distance diffusion coefficients than might apply to monomers of proteins in crowded and dense environments. The relaxation rate k_r for simulations of the penetrating solvent model with more frequent stochastic rotations, where $\Delta t = 0.013\tau$ and a monomer diffusion coefficient of $0.0045 \ell^2/\tau$, is shown in Fig. 12. The equilibration dynamics lead to the same equilibrium probabilities of the unbound state (data not shown). Unlike the equilibrium probability of



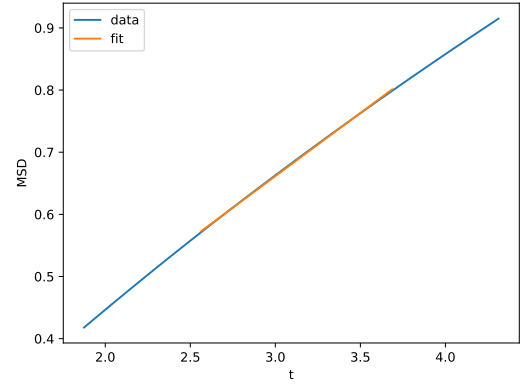
(a) Configurational probability of the unbound state vs. time for transition 1000000110 to 1010000110 in layer 3



(b) MSD for transition 1000000110 to 1010000110 in layer 3

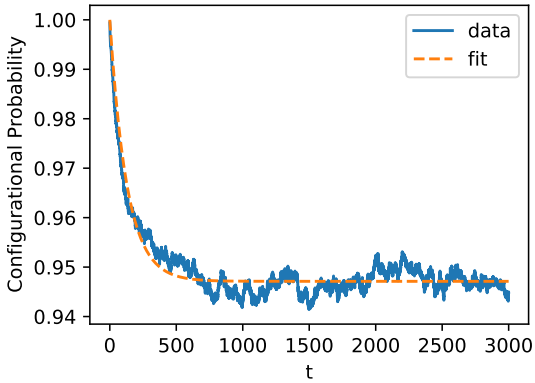


(c) Configurational probability of the unbound state vs. time for transition 1111001111 to 1111101111 in layer 8

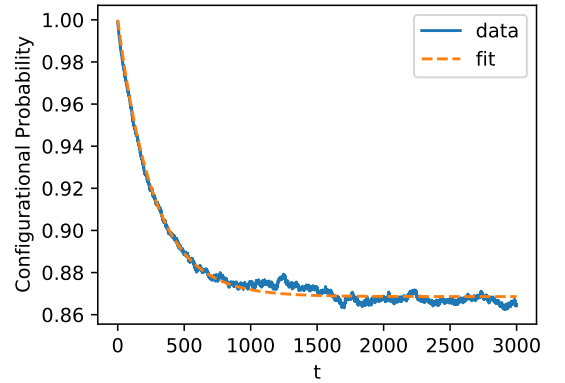


(d) MSD for transition 1111001111 to 1111101111 in layer 8

FIG. 7: A comparison of two different layers in the presence of the penetrating solvent at $\epsilon = 3.0$ with an ensemble of 10,000. The units for t in this figure, and in Figs. 8 and 9 are in simulation time units τ , where $\tau = \sqrt{m\ell^2/(k_B T)}$.

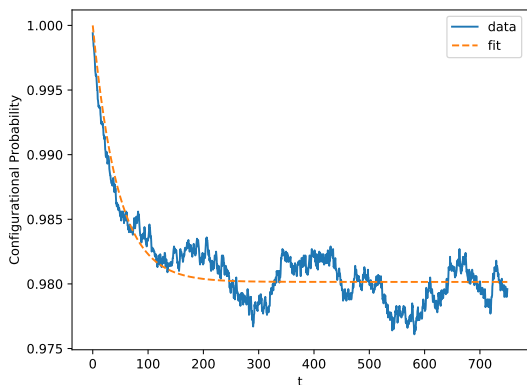


(a) Configurational probability of the unbound state vs. time at $\epsilon = 4.0$

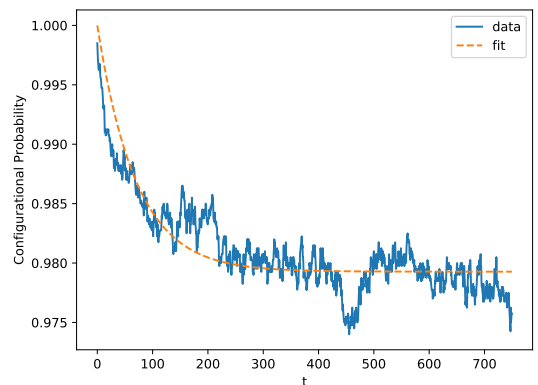


(b) Configurational probability of the unbound state vs. time at $\epsilon = 5.0$

FIG. 8: A comparison of two values of ϵ for layer 3 in the presence of the penetrating solvent with an ensemble size of $N_e = 10,000$.



(a) Configurational probability of the unbound state vs. time in the presence of the MPCD solvent with an ensemble size of $N_e = 10,000$



(b) Configurational probability of the unbound state vs. time in the presence of the hard-sphere solvent with an ensemble size of $N_e = 4,000$

FIG. 9: A comparison of the MPCD and hard-sphere solvent models for layer 3 at $\epsilon = 3.0$.

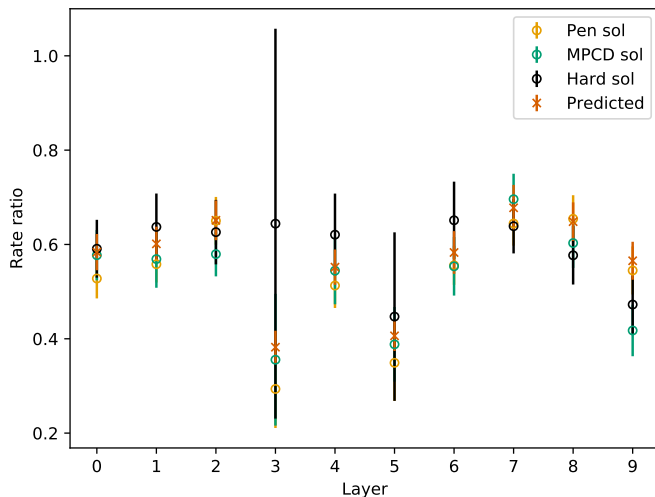


FIG. 10: The rate ratios, $k_r(4)/k_r(3)$, for crambin for all three solvent models.

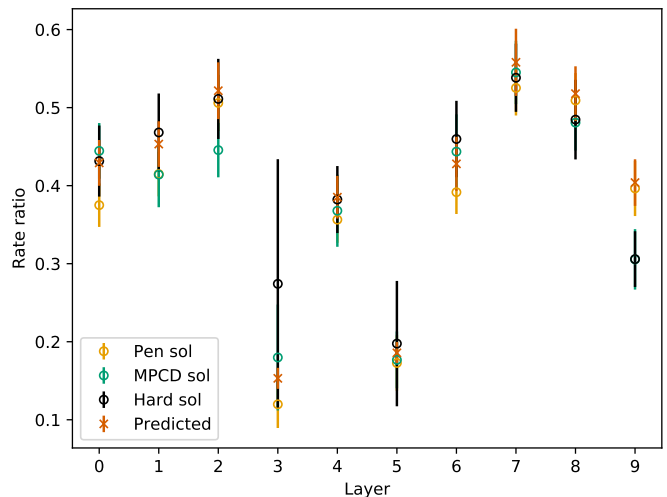


FIG. 11: The rate ratios, $k_r(5)/k_r(3)$, for crambin for all three solvent models.

the unbound state, n_u^{eq} , which is independent of the dynamics, there is a clear difference in the two sets of values of the decay rate k_r when comparing Fig. 12 to Fig. 4. As predicted, the decay constant k_r for each layer is considerably smaller than under the previous simulation parameters since the diffusion coefficient for a single bead is smaller by a factor of roughly 20. Nonetheless, the confidence intervals for the predicted rates, which differ from the previous values by the ratio of their diffusion coefficients, and those obtained from the simulations, overlap for all layers. The same trends in the rates relative to the layer have been confirmed.

Simulations of more viscous MPCD and hard-sphere fluids are numerically demanding, requiring prohibitively long computational times. For example, for the more dilute solvent simulations of layer 2, where $D_{(ij)} = 0.03 \ell^2/\tau$ and a fixed ensemble size of 10^5 was used, the

MPCD and hard-sphere simulations required a factor of 44 and 300 times more simulation time than the penetrating solvent simulations, respectively. The relative computational demand of the different solvents is expected to be much larger for more viscous fluids, particularly for the hard-sphere solvent, in which the collision frequency of solvent particles scales quadratically with the density.

VII. DISCUSSION AND CONCLUSIONS

In this work, we have confirmed that the diffusive Markov state model of a linear chain of the crambin protein in solution accurately predicts the rates of transitions between connected macrostates for three different solvent models and different choices of bond energies (relative to the temperature). By construction, the solvent models, which differ in the complexity and the computational

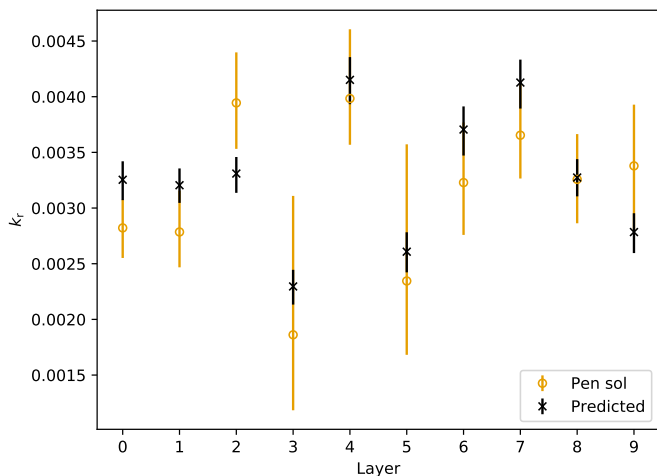


FIG. 12: The relaxation rate k_r for crambin for the penetrating solvent model at $\epsilon = 3.0$ with $N_e = 10^5$ when $\Delta t = 0.013\tau$ and the monomer diffusion coefficient is $D = 0.0045 \ell^2/\tau$.

demand of their simulation by orders of magnitude, provide a dissipative, fluctuating environment for the chain's monomers without influencing the macrostates' probabilities. The simulation results suggest that neither solvent-mediated hydrodynamic interactions between monomers nor the structural ordering of the solvent particles are important factors in the transition rates for the density of the solvents considered here. In the low-density hard-sphere solvent (volume fraction of 0.04), due to their small sizes of the solvent radii (0.1ℓ) and of the monomer beads (0.4ℓ), the radial distribution function at contact between the beads and the solvent, $g(R) \sim 1$, is not large, and little structural effect is expected until much higher volume fractions of hard-spheres. Solvent structural effects are not anticipated to be important unless there is strong ordering in the solvent around the protein chain and the solvent molecules are capable of stabilizing configurations. The hydrodynamic effects are much more difficult to estimate theoretically, even for a single solvated bead²⁴. The Stokes form for the hydrodynamic friction, which can be derived for a large massive Brownian particle whose $R \gg \xi$, where ξ is the scale on which the radial distribution varies, does not apply for the mesoscale-sized beads used in this work to represent a coarse-grained amino acid²⁶. This difficulty forces us to rely on numerical simulations of an isolated bead to establish the equivalence of the self-diffusion coefficient of a monomer in each of the solvents.

The only input from the equilibrium dynamics required in the diffusive Markov state model is the bond distance diffusion coefficients, $D_{(ij)}$. This transport property can be estimated from the rapid decay of the velocity autocorrelation function or from linear fits of the short-time dynamics of the mean-squared displacement. Both quantities do not require long trajectories and are not computationally intensive, though their evaluation is complicated

by mode coupling and other solvent effects. Ideally, we would like to be able to predict $D_{(ij)}$ from kinetic theory, but this is a daunting task since the rapid local hard interactions between the nearest and next-nearest monomers in the chain contribute to an internal friction that dominates over the friction induced by monomer-solvent interactions since $D_{(ij)}$ differs substantially from $2D_0$. Little kinetic theory work has been performed on models in which particles are bound to one another through geometrical constraints, and how to construct such a theory is an open question.

Another strong indication of the validity of the diffusion model is the confirmation that the predicted ratios of the equilibration rates for different bond energies, or, equivalently, the temperature, scale inversely with the ratio of the equilibrium populations of the bound state n_b^{eq} for the respective bond energy ϵ . The predicted rate ratios, which are independent of the bond diffusion coefficient $D_{(ij)}$, are quantitatively accurate for all layers and all three solvent models. Furthermore, the rates obtained from the simulations themselves scale with $D_{(ij)}$, as predicted by the diffusive Markov state model.

The success of the diffusive Markov state model for low-density solvents suggests that the local interactions among monomers provide sufficient friction for the motion of individual monomers, and the distances between them to be diffusive in nature. The solvent and the chain are weakly coupled, and the solvent-monomer interactions redistribute energy and effectively thermostat the chain. Although it is debatable whether a lower or higher-density solvent is more appropriate given the typical monomer size in the coarse-grained model, we expect that increasing the solvent friction by increasing the density should not alter the diffusive dynamics of monomers. This was confirmed for the penetrating solvent model, for which the simulation of a solvated model protein is not computationally prohibitive. However, higher-density solvents may allow for dynamical, solvent-mediated correlations to perturb the diffusive dynamics of the bonding distance.

In real solvents, such as water, solvent molecules can stabilize structures in a protein via local hydrogen-bonding and electrostatic interactions⁴⁷. Although such interactions are not included in the model, they could be incorporated by modeling solvent-monomer interactions with square-well potentials, as is performed for the nonlocal interactions among monomers in the chain. In such a model, the role of solvent interactions in conformational changes⁴⁸ could be analyzed using the diffusive Markov state model. In the model studied here, hydrophobic collapse⁴⁹⁻⁵¹ and other phenomena driven by solvent-solvent interactions⁵² can only be incorporated in a mean-field fashion through configurationally-dependent site energies¹⁶.

As discussed previously¹⁶, the simplicity of the temperature and site energy dependence of the transition matrix in the diffusive Markov state model enables not only the analysis of the mechanistic pathways between two spec-

ified configurations and how this pathway changes with temperature but also how site energies may be selected to optimize dynamical properties, such as the average passage time between two chosen states. Since the rate ratios for different choices of site energies are independent of $D_{(ij)}$, as has been confirmed here by the molecular dynamics simulations, the optimization of site energies can be carried out for a fixed set of values of the bond distance diffusion coefficient.

ACKNOWLEDGMENTS

Financial support from the National Sciences and Engineering Research Council of Canada is gratefully acknowledged. Computations were performed on the Cedar supercomputer at Simon Fraser University, which is funded by the Canada Foundation for Innovation under the auspices of the Digital Research Alliance of Canada, WestGrid, and Simon Fraser University. Code for this project is available at <https://github.com/margaritacolberg>. The authors acknowledge Vigneshwar Rajesh for assistance in coding and data analysis of the Markov state model.

Appendix A: DECAY RATES AND FIRST PASSAGE TIMES

For a two-state model in which a single bond between a pair of nonlocal beads can form and break at a distance r_c , under certain conditions, the dynamics of the non-equilibrium evolution of the population $n_u(t)$ of a configuration u , given by the average of the indicator function $\mathbb{1}_u(\mathbf{r})$ over the non-equilibrium density $P(\mathbf{r}, \mathbf{p}, t)$ at the phase space point (\mathbf{r}, \mathbf{p}) of the linear chain of beads, can be reasonably well approximated by a single exponential decay from an initial value of $n_u(0)$ to an equilibrium value n_u^{eq} of the form

$$\delta n_u(t) = n_u(t) - n_u^{\text{eq}} = \delta n_u(0)e^{-k_r t}, \quad (\text{A1})$$

where k_r is the characteristic rate of decay. Here, we choose the state u to differ from a state b by a single bond of length r , which is formed by the passage between unbonded configurations u that satisfy $r > r_c$ to bonded configurations satisfying $r < r_c$ while all other distance constraints are met, so that

$$\begin{aligned} n_u(t) &= \int' dr d\mathbf{p} H(r - r_c) P(\mathbf{r}, \mathbf{p}, t) \\ &= \int dr d\mathbf{p} H(r - r_c) \rho(r, \mathbf{p}, t). \end{aligned} \quad (\text{A2})$$

In Eq. (A2), $H(r - r_c)$ is the Heaviside function, and the prime on the integral indicates that all other distance constraints are maintained. Additionally, $\rho(r, \mathbf{p}, t)$ is the probability density obtained by integrating the full phase space density $P(\mathbf{r}, \mathbf{p}, t)$ over all but the bonding degrees of freedom. Here, we assume that the linear chain of beads is immersed in a stochastic environment due to the

presence of either an effective solvent (in the case of the penetrating model), a mesoscale solvent, or an explicit solvent. If the solvent degrees of freedom evolve rapidly on the timescale of the motion of the beads (for example, in the Brownian limit, in which the mass ratio of the solvent and bead particles is $m/M \ll 1$), the dynamics of the density of the reactive coordinate r and its conjugate momentum p can be written as⁵³

$$\partial_t \rho(r, p, t) = \mathcal{L}_{\text{fp}} \rho(r, p, t), \quad (\text{A3})$$

where \mathcal{L}_{fp} is an effective Fokker-Planck operator

$$\begin{aligned} \mathcal{L}_{\text{fp}} &= -p/M \partial_r + \partial_r u(r) \partial_p + \gamma \partial_p (\partial_p + \beta p/M) \\ &\quad + \hat{T}_R \delta(r - r_c). \end{aligned} \quad (\text{A4})$$

In Eq. (A4), \hat{T}_R is a collision operator that accounts for the step potential at $r = r_c$, in which the beads undergo an elastic collision when $p_c > p > 0$ or experience an impulse that results in a discontinuous jump in the momentum $p' = p \pm p_c$, where $p_c = \sqrt{\epsilon/(2M)}$ for a bond energy of ϵ . In (A4), γ is the friction acting on the bonding beads that arises from the interactions with the solvent and with other local beads, and $u(r)$ is the continuous and smooth potential of mean force. In order for the population dynamics to obey simple exponential behavior as in Eq. (A1), the solvent interactions must provide sufficient dissipation to establish a separation of timescale between transitions between states and the timescale of equilibration within each configuration.

The general solution of Eq. (A3) is difficult but can be accomplished by evaluating numerically the spectral decomposition of the Fokker-Planck operator: The discontinuity at $r = r_c$ requires separating the solution into spatial regions with $r < r_c$ and $r > r_c$ and matching the solutions at the point of discontinuity. If one breaks the solution into two ‘‘bulk’’ regions, $\rho^\pm(r, p, t)$, which are spatially removed from the transition region, and an interfacial region of width 2σ ,

$$\begin{aligned} \rho(r, p, t) &= \rho^s(r, p, t) + \rho^+(r, p, t) H(r - r_c - \sigma) \\ &\quad + \rho^-(r, p, t) H(r_c - \sigma - r), \end{aligned} \quad (\text{A5})$$

the dynamics of the density in the bulk regions is simple, while the dynamics of $\rho^s(r, p, t)$ in the interfacial region is complicated by the effect of the impulses that lead to a non-Boltzmann distribution of the momentum^{54,55}. In the thin interfacial region approximation corresponding to the limit $\sigma \rightarrow 0$, the solutions of ρ^\pm are extended to the transition state $r = r_c$. Using techniques similar to the multipole expansions of excess surface densities in hydrodynamics^{56,57}, in the thin layer approximation, the effect of the metastable region can be replaced by a boundary condition on the equations for the bulk densities, $\rho^\pm(r, p, t)$ ⁵⁷.

In the high friction limit, where the distribution of momentum relaxes quickly to the Boltzmann distribution in all spatial regions, one expects that the dynamics of ρ can be reduced to the Smoluchowski equation, in which the

marginal density $\rho(r, t) = \int dp \rho(r, p, t)$ obeys the diffusion equation^{18,58},

$$\partial_t \rho(r, t) = \mathcal{L} \rho(r, t), \quad (\text{A6})$$

where \mathcal{L} is defined as

$$\mathcal{L} = D \partial_r e^{-\beta u(r)} \partial_r e^{\beta u(r)}, \quad (\text{A7})$$

and $D = (\beta^2 \gamma)^{-1}$. Continuity of probability leads to the jump conditions¹⁸

$$\partial_r \rho(r, t) \Big|_{r_c^-} = \partial_r \rho(r, t) \Big|_{r_c^+}, \quad (\text{A8})$$

$$e^{\beta u(r_c^+)} \rho(r_c^+, t) = e^{\beta u(r_c^-)} \rho(r_c^-, t). \quad (\text{A9})$$

For the diffusive system, the characteristic decay time k_r^{-1} in Eq. (A1) can be expressed as a one-dimensional integral. For a system with reflecting boundaries at $r = a$ and $r = b$,

$$\begin{aligned} \delta n_u(t) &= \int_a^b dr H(r - r_c) (\rho(r, t) - \rho_e(r)) \\ &= \int_a^b dr H(r - r_c) e^{\mathcal{L}t} \mathcal{Q} \rho(r, 0) \\ &= \int_a^b dr dr_0 \rho(r_0, 0) H(r - r_c) e^{\mathcal{L}t} \mathcal{Q} \delta(r - r_0) \\ &= \int_a^b dr dr_0 \rho(r_0, 0) H(r - r_c) e^{\mathcal{Q} \mathcal{L}t} \mathcal{Q} \delta(r - r_0), \end{aligned} \quad (\text{A10})$$

where $\rho_e(r)$ is the equilibrium density satisfying $\mathcal{L} \rho_e(r) = 0$, and \mathcal{Q} is a projection operator that removes the projection onto the equilibrium density⁵⁹, $\mathcal{Q} G(r) = G(r) - \rho_e(r) \int_a^b dx G(x)$. From the Laplace transform $\delta \tilde{n}_u(z)$ of Eq. (A2), one has $k_r^{-1} = \lim_{z \rightarrow 0} \delta \tilde{n}_u(z) / \delta n_u(0)$, hence

$$\begin{aligned} k_r^{-1} \delta n_u(0) &= \int_a^b dr dr_0 \rho(r_0, 0) H(r - r_c) (-\mathcal{Q} \mathcal{L})^{-1} \mathcal{Q} \delta(r - r_0) \\ &= \int_a^b dr dr_0 \rho(r_0, 0) H(r - r_c) \mu_{-1}(r, r_0), \end{aligned} \quad (\text{A11})$$

where $\mu_{-1}(r, r_0) = -[\mathcal{Q} \mathcal{L} \mathcal{Q}]^{-1} \delta(r - r_0)$ or $\mathcal{Q} \mathcal{L} \mu_{-1}(r, r_0) = -\mathcal{Q} \delta(r - r_0)$. Direct integration of this equation gives

$$\mu_{-1}(r, r_0) = D^{-1} J(r, r_0) - D^{-1} \rho_e(r) \int_a^b dr' J(r', r_0), \quad (\text{A12})$$

where

$$\begin{aligned} J(r, r_0) &= H(r_c - r) \rho_b(r) \int_r^{r_c} dy \frac{H(y - r_0) - n_b C_b(y)}{\rho_b(r)} \\ &+ H(r - r_c) \rho_u(r) \int_{r_c}^r dy \frac{H(r_0 - y) - n_u (1 - C_u(y))}{\rho_u(r)}. \end{aligned}$$

Here, $n_u^{\text{eq}} \rho_u(r) = H(r - r_c) \rho_e(r)$ defines the conditional equilibrium density $\rho_u(r)$ in the unbonded state, $C_u(r) =$

$\int_{r_c}^r dy \rho_u(y)$ is the cumulative distribution of $\rho_u(r)$, and $\rho_b(r)$ and $C_b(r)$ are similarly defined. Inserting Eq. (A12) into Eq. (A11) gives

$$k_r^{-1} \delta n_u(0) = \int_a^b dr_0 \rho(r_0, 0) (n_b^{\text{eq}} \gamma_2(r_0) - n_u^{\text{eq}} \gamma_1(r_0)), \quad (\text{A13})$$

where

$$\gamma_1(r_0) = D^{-1} \int_a^{r_c} J(r, r_0) \quad (\text{A14})$$

$$= \frac{H(r_c - r_0)}{D} \int_{r_0}^{r_c} dy \frac{C_b(y)}{\rho_b(y)} - n_b^{\text{eq}} \tau_b,$$

$$\gamma_2(r_0) = D^{-1} \int_{r_c}^b J(r, r_0) \quad (\text{A15})$$

$$= \frac{H(r_0 - r_c)}{D} \int_{r_c}^{r_0} dy \frac{1 - C_u(y)}{\rho_u(y)} - n_u^{\text{eq}} \tau_u,$$

and τ_b and τ_u are the inner and outer average first passage times

$$\begin{aligned} \tau_b &= \frac{1}{D} \int_a^{r_c} dr \frac{C_b(r)^2}{\rho_b(r)}, \\ \tau_u &= \frac{1}{D} \int_{r_c}^b dr \frac{(1 - C_u(r))^2}{\rho_u(r)}. \end{aligned} \quad (\text{A16})$$

Finally, for the special case in which the initial value of r_0 is distributed according to the conditional equilibrium distribution,

$$\rho(r_0, 0) = \left[\frac{n_b(0)}{n_b^{\text{eq}}} H(r_c - r_0) + \frac{n_u(0)}{n_u^{\text{eq}}} H(r_0 - r_c) \right] \rho_e(r_0), \quad (\text{A17})$$

$$\begin{aligned} k_r^{-1} &= \mu_{-1} / \delta n_u(0) \\ &= n_u^{\text{eq}} \tau_b + n_b^{\text{eq}} \tau_u, \end{aligned} \quad (\text{A18})$$

which is equivalent to Eq. (6) in the main text.

In some cases, the decay of populations to equilibrium is not well-described by a single exponential for diffusive processes. It is often found that although the overall relaxation time is well-described by Eq. (A18), the initial decay is faster and the later decay is slower than that predicted by the single exponential approximation. If desired, more accurate relaxation profiles can be constructed by higher-order Padé approximations⁵⁹⁻⁶¹,

$$\begin{aligned} \delta n_u(t) / \delta n_u(0) &= \frac{1}{t_1 - t_2} \left(t_1 e^{-t/t_1} - t_2 e^{-t/t_2} \right) \\ &- \frac{\mu_1 t_1 t_2}{t_2 - t_1} \left(e^{-t/t_1} - e^{-t/t_2} \right). \end{aligned} \quad (\text{A19})$$

Here, $\mu_1 = -\delta \dot{n}_u(0)$ is the initial rate of decay of $\delta n_u(t)$, given by the average initial flux at the transition state

position $r = r_c$, and the timescale parameters satisfy

$$\begin{aligned}\mu_{-1}/\delta n_u(0) &= t_1 + t_2 - \mu_1 t_1 t_2 = n_u^{\text{eq}} \tau_b + n_b^{\text{eq}} \tau_u, \\ \mu_{-2}/\delta n_u(0) &= \int_0^{\infty} dt t \delta n_u(t)/\delta n_u(0) \\ &= t_1^2 + t_1 t_2 + t_2^2 - \mu_1 t_1 t_2 (t_1 + t_2),\end{aligned}\quad (\text{A20})$$

where

$$\begin{aligned}\mu_{-2} &= \int_a^b dr H(r - r_c) \mu_{-2}(r) \\ &= \delta n_u(0) (n_u^{\text{eq}} \tau_{2b} + n_b^{\text{eq}} \tau_{2u} - n_u^{\text{eq}} n_b^{\text{eq}} (\tau_b - \tau_u)^2),\end{aligned}\quad (\text{A21})$$

and

$$\begin{aligned}\tau_{2b} &= \frac{1}{D^2} \int_a^{r_c} dr \rho_b(r) \left(\int_r^{r_c} dx \frac{C_b(x)}{\rho_b(x)} \right)^2, \\ \tau_{2u} &= \frac{1}{D^2} \int_{r_c}^b dr \rho_u(r) \left(\int_{r_c}^r dx \frac{1 - C_u(x)}{\rho_u(x)} \right)^2,\end{aligned}\quad (\text{A22})$$

a result that can be obtained in a similar manner to that used to derive Eq (A12) by integrating the equation $\mathcal{Q}\mathcal{L}\mu_{-2}(r) = -\mu_{-1}(r)$ and using reflecting boundary conditions at the limits a and b .

We remark that all these results depend on several approximations: first, the force exerted by the solvent on the beads is rapid on the timescale of the bead motion. Second, the bead dynamics is overdamped and diffusive in all regions, maintaining an equilibrium distribution of the relative momentum of the bonding beads. Finally, there is a separation of timescale between the time required to reach a conditional equilibrium in each of the configurations and the time required to change from one bonding configuration to another.

- ¹T. J. Lane, D. Shukla, K. A. Beauchamp, and V. S. Pande, *Curr. Opin. Struct. Biol.* **23**, 58 (2013).
- ²S. A. Hollingsworth and R. O. Dror, *Neuron* **99**, 1129 (2018).
- ³J. D. Chodera and F. Noé, *Curr. Opin. Struct. Biol.* **25**, 135 (2014).
- ⁴D. E. Shaw, M. M. Deneroff, R. O. Dror, J. S. Kuskin, R. H. Larson, J. K. Salmon, C. Young, B. Batson, K. J. Bowers, J. C. Chao, M. P. Eastwood, J. Gagliardo, J. P. Grossman, C. R. Ho, D. J. Ierardi, I. Kolossváry, J. L. Klepeis, T. Layman, C. McLeavey, M. A. Moraes, R. Mueller, E. C. Priest, Y. Shan, J. Spengler, M. Theobald, B. Towles, and S. C. Wang, *Commun. ACM* **51**, 91 (2008).
- ⁵F. Noé, C. Schütte, E. Vanden-Eijnden, L. Reich, and T. Weikl, *Proc. Natl. Acad. Sci. U. S. A.* **106**, 19011 (2009).
- ⁶V. S. Pande, K. Beauchamp, and G. R. Bowman, *Methods* **52**, 99 (2010).
- ⁷W. Wang, S. Cao, L. Zhu, and X. Huang, *Wiley Interdiscip. Rev.: Comput. Mol. Sci.* **8**, e1343 (2018).
- ⁸B. E. Husic and V. S. Pande, *J. Am. Chem. Soc.* **140**, 2386 (2018).
- ⁹K. A. Konovalov, I. C. Unarta, S. Cao, E. C. Goonetilleke, and X. Huang, *JACS Au* **1**, 1330 (2021).
- ¹⁰A. Mardt, T. Hempel, C. Clementi, and F. Noé, *Nat. Commun.* **13**, 7101 (2022).
- ¹¹G. R. Bowman, K. A. Beauchamp, G. Boxer, and V. S. Pande, *J. Chem. Phys.* **131**, 124101 (2009).

- ¹²J.-H. Prinz, H. Wu, M. Sarich, B. Keller, M. Senne, M. Held, J. D. Chodera, C. Schütte, and F. Noé, *J. Chem. Phys.* **134**, 174105 (2011).
- ¹³B. Trendelkamp-Schroer, H. Wu, F. Paul, and F. Noé, *J. Chem. Phys.* **143**, 174101 (2015).
- ¹⁴M. von Kleist, C. Schütte, and W. Zhang, *J. Stat. Phys.* **170**, 809 (2018).
- ¹⁵D. J. Sharpe and D. J. Wales, *Phys. Rev. E* **104**, 015301 (2021).
- ¹⁶M. Colberg and J. Schofield, *J. Chem. Phys.* **157**, 125101 (2022).
- ¹⁷H. B. Movahed, R. van Zon, and J. Schofield, *J. Chem. Phys.* **136**, 245103 (2012).
- ¹⁸J. Schofield and H. Bayat, *J. Chem. Phys.* **141**, 095101 (2014).
- ¹⁹S. Duane, A. D. Kennedy, B. J. Pendleton, and D. Roweth, *Phys. Lett. B* **195**, 216 (1987).
- ²⁰A. Schmidt, M. Teeter, E. Weckert, and V. S. Lamzin, *Acta Crystallogr. Sect. F: Struct. Biol. Cryst. Commun.* **67**, 424 (2011).
- ²¹C. Jelsch, M. M. Teeter, V. Lamzin, V. Pichon-Pesme, R. H. Blessing, and C. Lecomte, *Proc. Natl. Acad. Sci. U. S. A.* **97**, 3171 (2000).
- ²²M. M. Teeter and W. A. Hendrickson, *J. Mol. Biol.* **127**, 219 (1979).
- ²³J. Schofield, *J. Phys. Chem. B* **121**, 6847 (2017).
- ²⁴J. T. Hynes, R. Kapral, and M. Weinberg, *J. Chem. Phys.* **70**, 1456 (1979).
- ²⁵B. J. Alder and T. E. Wainwright, *Phys. Rev. A* **1**, 18 (1970).
- ²⁶J. Schofield and I. Oppenheim, *Phys. A: Stat. Mech. Appl.* **187**, 210 (1992).
- ²⁷W. Sung and G. Stell, *J. Chem. Phys.* **77**, 4636 (1982).
- ²⁸C. M. Silva, H. Liu, and E. A. Macedo, *Ind. Eng. Chem. Res.* **37**, 221 (1998).
- ²⁹L. Bocquet, J. Piasecki, and J.-P. Hansen, *J. Stat. Phys.* **76**, 505 (1994).
- ³⁰L. Bocquet, J.-P. Hansen, and J. Piasecki, *J. Stat. Phys.* **76**, 527 (1994).
- ³¹A. T. Celebi, S. H. Jamali, A. Bardow, T. J. H. Vlught, and O. A. Moulto, *Mol. Simul.* **47**, 831 (2021).
- ³²G. Gompper, T. Ihle, D. M. Kroll, and R. G. Winkler, “Multi-particle collision dynamics: A particle-based mesoscale simulation approach to the hydrodynamics of complex fluids,” in *Advanced Computer Simulation Approaches for Soft Matter Sciences III*, edited by C. Holm and K. Kremer (Springer Berlin, Heidelberg, 2009) p. 1.
- ³³D. Viduna and W. R. Smith, *Mol. Phys.* **100**, 2903 (2002).
- ³⁴A. Malevanets and R. Kapral, *J. Chem. Phys.* **110**, 8605 (1999).
- ³⁵A. Malevanets and R. Kapral, *J. Chem. Phys.* **112**, 7260 (2000).
- ³⁶R. Kapral, *Adv. Chem. Phys.* **140**, 89 (2008).
- ³⁷J. Schofield, P. Inder, and R. Kapral, *J. Chem. Phys.* **136**, 205101 (2012).
- ³⁸T. Ihle and D. M. Kroll, *Phys. Rev. E* **63**, 020201 (2001).
- ³⁹T. Ihle and D. M. Kroll, *Phys. Rev. E* **67**, 066705 (2003).
- ⁴⁰M. Abramowitz and I. A. Stegun, *Handbook of Mathematical Functions with Formulas, Graphs, and Mathematical Tables* (Dover, 1965).
- ⁴¹D. Brune and S. Kim, *Proc. Natl. Acad. Sci. U. S. A.* **90**, 3835 (1993).
- ⁴²H. Walderhaug, O. Söderman, and D. Topgaard, *Prog. Nucl. Magn. Reson. Spectrosc.* **56**, 406 (2010).
- ⁴³R. Evans, G. Dal Poggetto, M. Nilsson, and G. A. Morris, *Anal. Chem.* **90**, 3987 (2018).
- ⁴⁴B. Tang, K. Chong, W. Masefski, and R. Evans, *J. Phys. Chem. B* **126**, 5887 (2022).
- ⁴⁵N. Nemoto, Y. Makita, Y. Tsunashima, and M. Kurata, *Macromolecules* **17**, 425 (1984).
- ⁴⁶B. Efron, *The Jackknife, the Bootstrap, and Other Resampling Plans*, CBMS-NSF Regional Conference Series in Applied Mathematics (Society for Industrial and Applied Mathematics, 1982).
- ⁴⁷M.-C. Bellissent-Funel, A. Hassanali, M. Havenith, R. Henchman, P. Pohl, F. Sterpone, D. van der Spoel, Y. Xu, and A. E. Garcia, *Chem. Rev.* **116**, 7673 (2016).
- ⁴⁸P. Prakash, A. Sayyed-Ahmad, and A. A. Gorfe, *PLoS Comput.*

- Biol. **8**, e1002394 (2012).
- ⁴⁹M. Brylinski, L. Konieczny, and I. Roterman, *Comput. Biol. Chem.* **30**, 255 (2006).
- ⁵⁰L. J. Lapidus, S. Yao, K. S. McGarrity, D. E. Hertzog, E. Tubman, and O. Bakajin, *Biophys. J.* **93**, 218 (2007).
- ⁵¹H. Wirtz, S. Schäfer, C. Hoberg, K. M. Reid, D. M. Leitner, and M. Havenith, *Biochemistry* **57**, 3650 (2018).
- ⁵²Q. Sun, *Molecules* **27**, 7009 (2022).
- ⁵³P. Mazur and I. Oppenheim, *Physica* **50**, 241 (1970).
- ⁵⁴S. V. G. Menon and D. C. Sahni, *Phys. Rev. A* **32**, 3832 (1985).
- ⁵⁵P. Kalinay and J. K. Percus, *J. Stat. Phys.* **148**, 1135 (2012).
- ⁵⁶D. Ronis, D. Bedeaux, and I. Oppenheim, *Physica A Stat. Mech. Appl.* **90**, 487 (1978).
- ⁵⁷B. Robertson, J. Schofield, and R. Kapral, (2024), 10.1063/5.0185361.
- ⁵⁸I. Oppenheim and J. McBride, *Physica A Stat. Mech. Appl.* **165**, 279 (1990).
- ⁵⁹W. Nadler and K. Schulten, *J. Chem. Phys.* **82**, 151 (1985).
- ⁶⁰A. Szabo, *J. Chem. Phys.* **72**, 4620 (1980).
- ⁶¹W. Nadler and K. Schulten, *Phys. Rev. Lett.* **51**, 1712 (1983).